CrossMark

ORIGINAL PAPER

Numerical Investigation of Seismically Induced Rock Mass Fatigue as a Mechanism Contributing to the Progressive Failure of Deep-Seated Landslides

Valentin Gischig[1] · Giona Preisig[1] · Erik Eberhardt[1]

Abstract The importance of earthquakes in triggering catastrophic failure of deep-seated landslides has long been recognized and is well documented in the literature. However, seismic waves do not only act as a trigger mechanism. They also contribute to the progressive failure of large rock slopes as a fatigue process that is highly efficient in deforming and damaging rock slopes. Given the typically long recurrence time and unpredictability of earthquakes, field-based investigations of co-seismic rock slope deformations are difficult. We present here a conceptual numerical study that demonstrates how repeated earthquake activity over time can destabilize a relatively strong rock slope by creating and propagating new fractures until the rock mass is sufficiently weakened to initiate catastrophic failure. Our results further show that the damage and displacement induced by a certain earthquake strongly depends on pre-existing damage. In fact, the damage history of the slope influences the earthquake-induced displacement as much as earthquake ground motion characteristics such as the peak ground acceleration. Because seismically induced fatigue is: (1) characterized by low repeat frequency, (2) represents a large amplitude damage event, and (3) weakens the entire rock mass, it differs from other fatigue processes. Hydro-mechanical cycles, for instance, occur at higher repeat frequencies (i.e., annual cycles), lower amplitude, and only affect limited parts of the rock mass. Thus, we also compare seismically induced fatigue to seasonal hydro-mechanical fatigue.

While earthquakes can progressively weaken even a strong, competent rock mass, hydro-mechanical fatigue requires a higher degree of pre-existing damage to be effective. We conclude that displacement rates induced by hydro-mechanical cycling are indicative of the degree of pre-existing damage in the rock mass. Another indicator of pre-existing damage is the seismic amplification pattern of a slope; frequency-dependent amplification factors are highly sensitive to changes in the fracture network within the slope. Our study demonstrates the importance of including fatigue-related damage history—in particular, seismically induced fatigue—into landslide stability and hazard assessments.

Keywords Deep-seated landslides · Seismic slope stability · Rock mass fatigue · Brittle fracture damage · Progressive failure · Numerical modeling

1 Introduction

Profound understanding of the relationship between destabilizing landslide processes and the rock mass response is a key topic in landslide analysis. It is essential for distinguishing between acceleration phases that are seasonal and innocuous, and those that indicate impending catastrophic failure. Hence, appropriate understanding of the landslide response to different forcing mechanisms (e.g., earthquake-induced deformations, groundwater pressure changes, toe erosion, etc.) can guide decisions on effective mitigation strategies (e.g., Eberhardt et al. 2007). Comprehensive monitoring systems recording slope deformation and environmental parameters (i.e., rainfall, temperature, ground water level, etc.) in connection with an early warning system have become a widely used tool to

✉ Valentin Gischig
gischig@sed.ethz.ch

[1] Geological Engineering, Department of Earth, Ocean, and Atmospheric Sciences, University of British Columbia, Vancouver, BC, Canada

manage the hazard posed by a landslide threatening civil infrastructure. However, the use of such monitoring systems goes beyond an alert to landslide acceleration events. It can provide baseline understanding of the episodic and time-dependent behavior of the slope and reveal the dominant driving mechanisms responsible for progressive failure of the rock mass (Eberhardt et al. 2004; Eberhardt 2008; Gischig et al. 2011a, b).

1.1 Slope-Scale Fatigue

Destabilization processes—also termed driving mechanisms—can be divided loosely into preparatory factors and triggering factors following the terminology by Gunzburger et al. (2005). The transition between preparatory factors and triggering factors may be gradual, but they can be seen as end members of a number of mechanisms acting on different time scales to deform and damage a rock mass, contributing to its progressive failure. Preparatory factors gradually change material strength and resisting forces (those inhibiting failure), or driving forces (i.e., those promoting failure) over long time periods (e.g., 10–100,000 years). Triggering factors are short-term changes of forces acting on time scales of seconds to a few years that ultimately lead to catastrophic slope failure. These processes are usually the reported causes of the catastrophic event. The concept is visualized in Fig. 1.

Driving mechanisms preparing or triggering catastrophic failure may include the following:

1. Seismic loading by local earthquakes.
2. Changes in water pressure due to rainfall, snowmelt, or water level changes of adjacent reservoirs.
3. Changes in slope geometry, e.g., due to natural erosion (glacial or fluvial) or slope engineering.
4. Cyclic temperature changes (i.e., thermal strains).
5. Freeze–thaw cycles.
6. Chemical weathering.
7. Micro-scale damage processes (e.g., creep of clay or gouge material, stress corrosion).
8. Wave impact or tidal forces on coastal cliffs.

The first five are considered in Fig. 1, which also shows that these mechanisms may act concurrently and interact with each other. For instance, repeated seismic loading has the potential to induce significant incremental damage in the form of brittle fracture propagation through intact rock bridges and accumulated dilation and slip along existing fractures, which accrue until the rock mass reaches a highly critical state (e.g., Welkner et al. 2010; Moore et al. 2012). At this point, a minor disturbance—a small earthquake or water pressure increase due to rainfall or snowmelt—may become the ultimate trigger of catastrophic failure. If the slope is in a sufficiently critical state, a pressure increase during an ordinary seasonal cycle may by enough to trigger failure (i.e., as depicted in Fig. 1). Some driving

Fig. 1 Role of driving mechanisms (here earthquakes, water pressure changes, slope geometry changes and thermo-elastic cycles) in altering driving and resisting forces within a potentially unstable rock mass (adapted from Gunzburger et al. 2005). Damage is accumulated by repeated load changes either as (seasonal) cycles or during stronger shorter term events
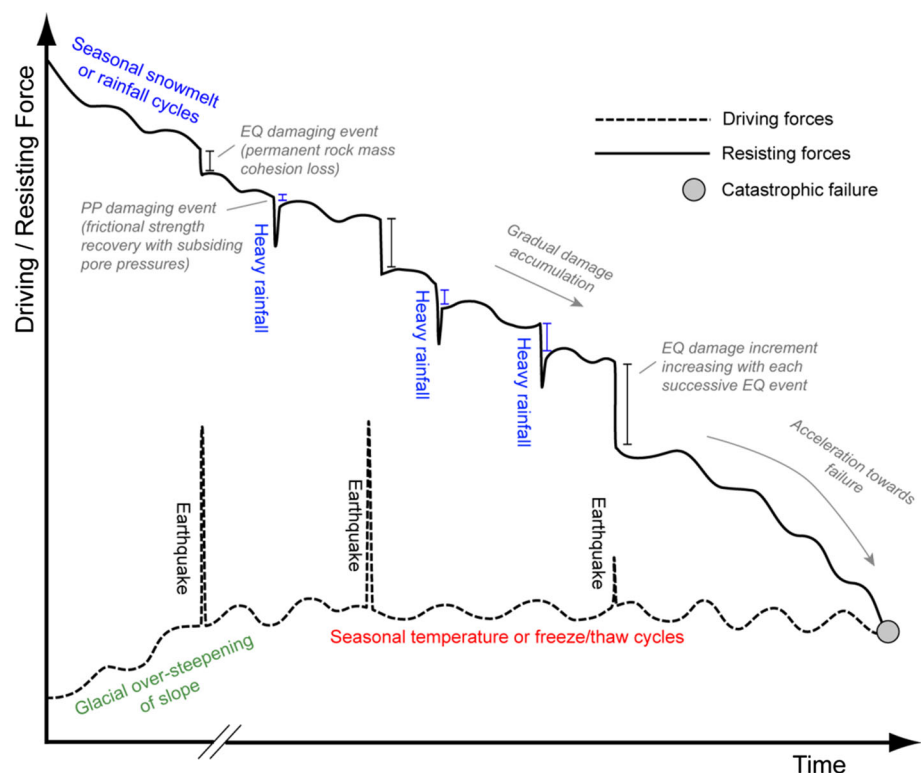
mechanisms are characterized by their cyclic or repeated nature (e.g., seasonal water pressure increases or temperature changes). Recently, cyclic or repeated loading as progressive weakening processes has been discussed in the literature as a large-scale fatigue process; e.g., seasonal pore pressure changes (Bonzanigo et al. 2007; Preisig et al. 2015), dam reservoir levels (Zangerl et al. 2010), or thermo-mechanical effects (Watson et al. 2004; Gunzburger et al. 2005; Gischig et al. 2011a, b; Bakun-Mazor et al. 2013). These examples of cyclic forcing mechanisms are analogous to fatigue observed in laboratory experiments in which rock samples are brought to failure as a consequence of cyclic load changes below the actual failure limit (Attewell and Farmer 1973; Xiao et al. 2009). Similar to other cyclic load changes, repeated seismic loading may be understood to be a high-amplitude, low-repeat frequency fatigue mechanism driving progressive failure over a very long time interval.

1.2 Seismic Loading as a Fatigue Mechanism

Seismic loading by local earthquake events is clearly one of the most important mechanisms for destabilizing landslides. Numerous cases of earthquake-induced landslides with dramatic consequences in terms of fatalities demonstrate the role of earthquakes as a triggering factor of catastrophic failure, for instance: 1959 Madison Canyon landslide and M_w7.3 Hebgen Lake earthquake in the USA (Hadley 1964; Wolter et al. 2015); 1970 Huascaran landslide and M_w7.8 Huaraz earthquake in Peru (Plafker and Ericksen 1978); 2001 Las Colinas landslide and M_w7.6 El Salvador earthquake in El Salvador (Evans and Bent 2004; Crosta et al. 2005); and the Chengxi and Donghekou landslides and M_w7.9 Wenchuan earthquake in China (Yin et al. 2011). The Wenchuan earthquake is a particularly devastating example of the destructive power of seismically induced landslides, as up to 30,000 landslide fatalities were recorded—one-third of the total earthquake fatalities. However, as illustrated in Fig. 1, earthquakes may not always lead directly to catastrophic slope failure, but may contribute to an incremental destabilization of a rock slope. Although the violent impact of earthquakes on slope stability is obvious from the large number of seismically induced landslides, their role in progressively damaging slopes and hence preparing them for catastrophic failure has been given little attention. This may be in part due to difficulties in quantifying damage resulting from repeated seismic loading, together with the infrequent reoccurrence rate of damaging earthquakes. As noted by Moore et al. (2011), co-seismic deformation is rarely recorded in monitoring data. Nevertheless, for many cases it was hypothesized that earthquakes had a role in weakening slopes for subsequent catastrophic failure.

One example is the Rawilhorn rock avalanche in Switzerland, 1946 (Figs. 2, 3a), which was not triggered by the primary M_w6.1 earthquake in Sierre, but by a M_w6.0 aftershock a few months later (Fritsche and Fäh 2009). Moore et al. (2012) suggested that the first earthquake weakened the rock mass, leaving it in a critical state for triggering during the second event. Bakun-Mazor et al. (2013) compared seismically induced to thermally induced displacements in a steep fractured cliff in Israel, and found that thermal effects may have deformed the slope more efficiently than past earthquakes. To our knowledge, they are the first to quantitatively compare different driving mechanisms in their impact on stability. Parker (2013) and Parker et al. (2013) also recognized the relevance of earthquakes in progressive failure and developed an advanced version of the well-known Newmark method (Newmark 1965) to also account for slope weakening induced by repeated earthquakes. Parker (2013) also lists earthquakes with substantial numbers of triggered landslides during the past 25 years. The Wenchuan earthquake in 2008 (M_w7.9) stands out due to the exceptional number of landslides it triggered (Huang and Fan 2013). Given the tectonic setting and history of repeated earthquakes in the Sichuan Province, including a M_w 7.5 event in 1933 and M_w 7.8 event in 1786 (Petley 2008), these may have led to an accumulation of damage that left many of the slopes in the region in a highly critical state, preconditioning them for catastrophic failure triggered by the 2008 earthquake.

Although direct observation of co-seismic deformation is difficult, there are examples of slope deformation that may be of seismic origin. Two examples from the southern Swiss Alps (Fig. 2) are presented in Fig. 3b, c. This region is characterized by high relief and glacially over-steepened rock slope faces (many of them dipping at angles >60°), which form steep slopes in pre-dominantly crystalline rocks; these are relatively stable where dominant discontinuity sets and foliation dip into the slope. However, along these slopes, there are many lineaments and open vertical tension cracks recounting strong past deformation. For the case of the Walkerschmatt slope shown in Fig. 3c, Yugsi Molina (2010) mentions that deformation monitoring has not shown any significant displacement over several years of monitoring. Structural properties of the rock mass indicate stable conditions; unrealistically low friction angles are required for failure to occur. Yet the slope is heavily deformed and shows deep, open sub-vertical tension cracks (Fig. 3c). In the case of Plattja located on the opposite valley flank (Fig. 3b), blocks are separated by sub-vertical tension fractures that have slipped along weak sub-horizontal foliation planes. Heynen (2010) applied the Newmark method to this case, and showed that slip induced by an M6 earthquake could well explain the observed deformations. The southern Swiss Alps are also characterized by intermediate seismic hazard
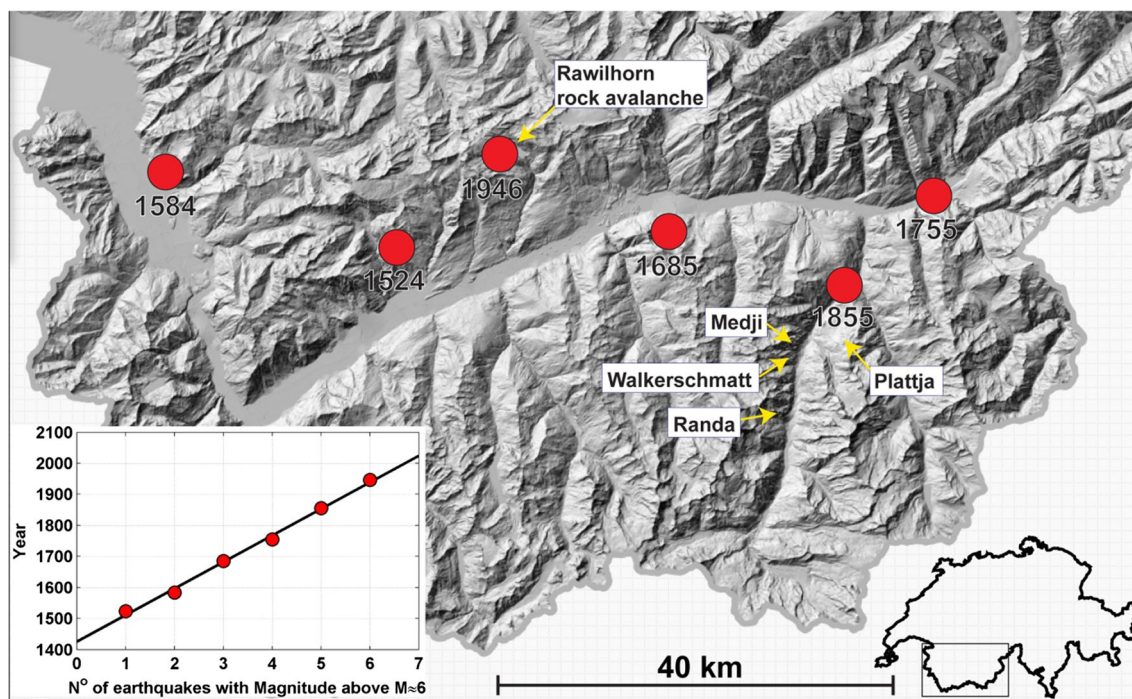
Fig. 2 Map of Valais in the south of Switzerland showing the epicenters of the last six earthquakes with magnitude $M \approx 6$ as retrieved from historic records (e.g., Fritsche et al. 2006; Fritsche and Fäh 2009; map reproduced from Fäh et al. 2012). Also indicated is the Rawilhorn rock avalanche triggered by earthquakes in 1946, the sites of the Randa 1991 slope failures, of the Medji 2002 slope failure, as well as of the deformed slopes at Walkerschmatt and Plattja

Fig. 3 **a** Photo of the Rawilhorn rock avalanche that was triggered by a $M_w6.0$ earthquake that occurred a few months after the $M_w6.1$ in 1946 (source: R. Mayoraz). **b** Aerial view of the Plattja slope (from Heynen 2010). Wide open fractures may be the result of past earthquakes (e.g., the 1855 earthquake in Visp, Fritsche et al. 2006). **c** Side and map view of the Walkerschmatt slope (adapted from Burjánek et al. 2012). Many of the fractures are open by centimeters to several decimeters (fracture network from Yugsi Molina 2010)
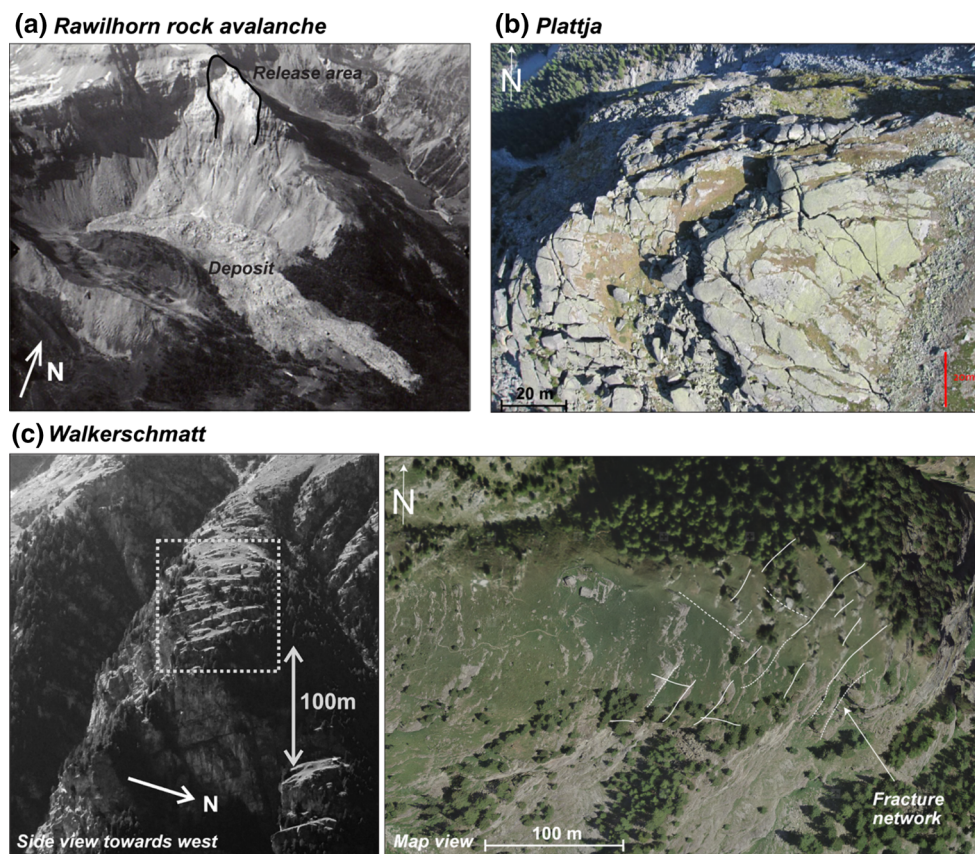
(Fäh et al. 2012). An earthquake with magnitude ∼M6 strikes this region about every 100 years on average (Fig. 2). In 1855, one of these earthquakes occurred a few kilometers north of the Walkerschmatt and Plattja slopes. After the earthquake, many rock falls were reported in this region (Fritsche et al. 2006). Hence, while other mechanisms may also have contributed to deformation of these slopes, such as glacial retreat or freeze–thaw cycles, it is likely that past earthquakes have induced substantial damage in these rock masses.

The steep western valley flanks of the Matter valley where the Walkerschmatt slope is located, also hosted two cases of recent catastrophic rock slope failures (Fig. 4): the 1991 Randa failure events (Schindler et al. 1993; Fig. 4a), and the 2002 Medji failure (Rovina 2005; Jörg 2008; Fig. 4b). The Randa rockslides occurred as two large failure events separated by a 3-week period (total volume of 30 Mm³), and involved the retrogressive collapse of a subvertical, 800-m-high crystalline rock face. The first of the two failures initiated along a persistent pre-existent fault dipping 30° out of the slope that acted as a sliding surface (Sartori et al. 2003). The case is particularly interesting because no clear triggering mechanism was found. The events did occur during the April and May snowmelt period; however, the 1991 snowmelt was not exceptional compared to previous years, and therefore does not constitute an obvious trigger (Schindler et al. 1993). Eberhardt et al. (2004) suggested that long-term processes progressively weakened the rock mass until it reached a critical state making it susceptible to the next snowmelt period. The Medji failure involved ∼70,000 m³ of crystalline rock. The slope failed catastrophically after a period of accelerated movement during intense rainfall in November 2002 (Jörg 2008). Although elevated water pressure would seem to be an obvious trigger for this failure, the question still arises as to what the long-term destabilization mechanisms leading to impending failure were.

We hypothesize here that repeated seismic loading by past local earthquake events has acted as a long-term progressive weakening mechanism (termed seismic fatigue) that led to strong deformations in the cases of Walkerschmatt and Plattja, and prepared catastrophic failure in the case of the Randa and Medji rockslides. Given the long reoccurrence time and the unpredictability of earthquakes, field-based investigations of seismically induced rock slope fatigue and damage are difficult. Under such constraints, numerical modeling presents a valuable tool. We present here a numerical investigation of seismically induced fatigue processes, in which a rock slope representative of the steep crystalline slopes encountered in the southern Swiss Alps (and elsewhere) is exposed to a

Fig. 4 **a** Photos of the rock slope above the village Randa before and after the two catastrophic failures that occurred on 18 April 1991 and 9 May 1991 [photos by J.D. Roullier (before) and V. Gischig (after)]. **b** Photos of the Medji rock slope before and after the catastrophic failure in November 2002 [Photos taken from Rovina (2005), copied from Jörg (2008), (before) and from Yugsi Molina (2010) (after)]

(a) *Randa rockslides, April/May 1991*

30° dipping failure surface
View towards west   Before first failure   After second failure

(b) *Medji rockslides, November 2002*

View towards west   Before failure   After failure

sequence of earthquakes. The modeled slope geometry is a generalization of topographic profiles of the aforementioned cases (Fig. 5). Real ground motion records from past earthquakes with magnitudes between M5.7 and 7.4 are used to demonstrate how repeated seismic loading progressively induces damage in strong and seemingly stable massive crystalline rock masses. We further investigate the interaction of two fatigue processes by exposing the slopes damaged by earthquakes to seasonal variations of pore pressures and hydro-mechanical fatigue (Sect. 6). Finally, using methods by Bourdeau and Havenith (2008) and Gischig et al. (2015), we show that the internal state of damage within a rock slope produces characteristic patterns of seismic wave amplification that can be observed in ambient noise recordings from field surveys (Sect. 7). These hold promise in providing a means to assess the damage state of a large rock slope in situ based on field observations.

2 Method

2.1 UDEC Modeling

Earthquake and hydro-mechanically induced damage and displacements are computed using the 2D distinct-element code UDEC (Cundall and Hart 1992; Itasca 2011). This numerical method allows one to explicitly model the discontinuum behavior. A "bonded block model" approach is used where first the problem domain is cut into an assemblage of blocks bounded by contacts. The blocks are assumed to be linear elastic and non-divisible. The contacts consist of springs that mimic fracture compliance in both the normal and shear directions. Next, contacts are defined as either representing existing discontinuities or intact rock bridges. Those representing existing discontinuities are capable of tensile opening or shear slip, depending on the localized stresses acting on the contact. Bonded contacts are used to represent intact rock bridges and potential fracture pathways (i.e., incipient fractures) along which brittle fracture can be explicitly simulated (Lorig and Cundall 1987). Fracture damage occurs when the predefined strength criterion (Coulomb slip with cohesion, friction and tensile cut-off) is exceeded. Upon failure irreversible dislocation occurs either through opening or as slip.

2.2 Model Setup

Figure 6 shows the model geometry chosen for our study. The assumptions underlying the different features of the model setup are described in the following:
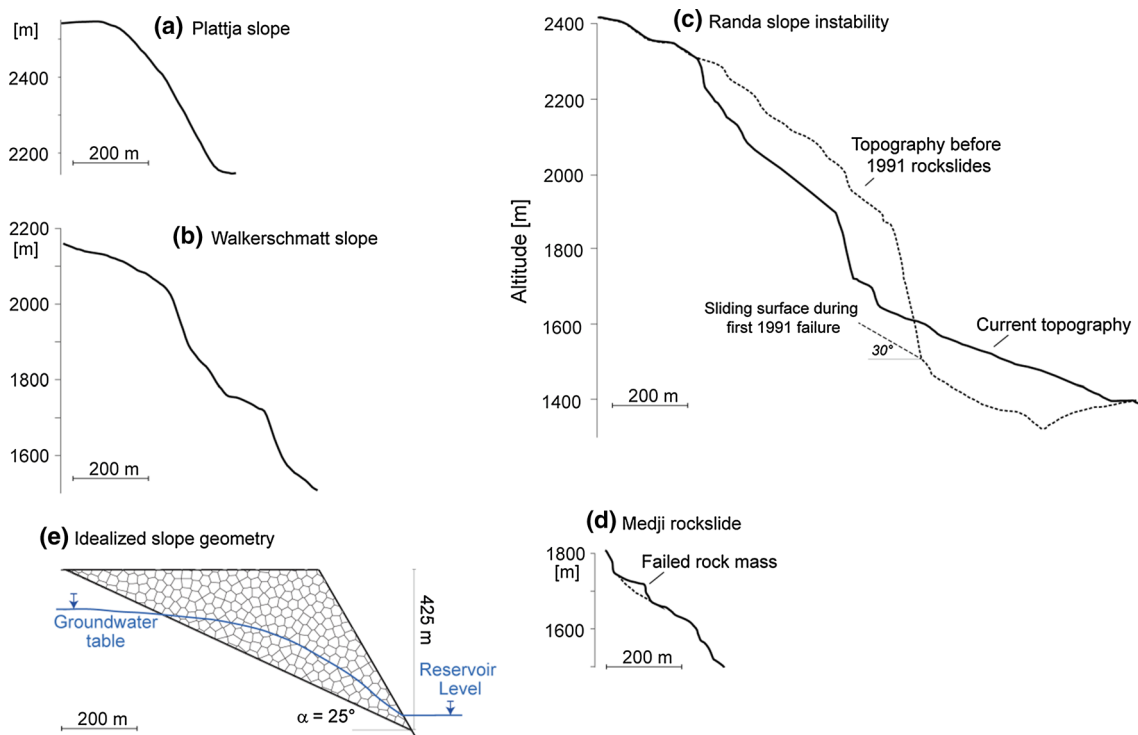

Fig. 5 Profiles of the aforementioned sites: **a** Plattja, **b** Randa, **c** Walkerschmatt, **d** Medji. **e** The generalized rock slope geometry including some features of these cases in a conceptual manner. Note that all slope profiles share the same scale

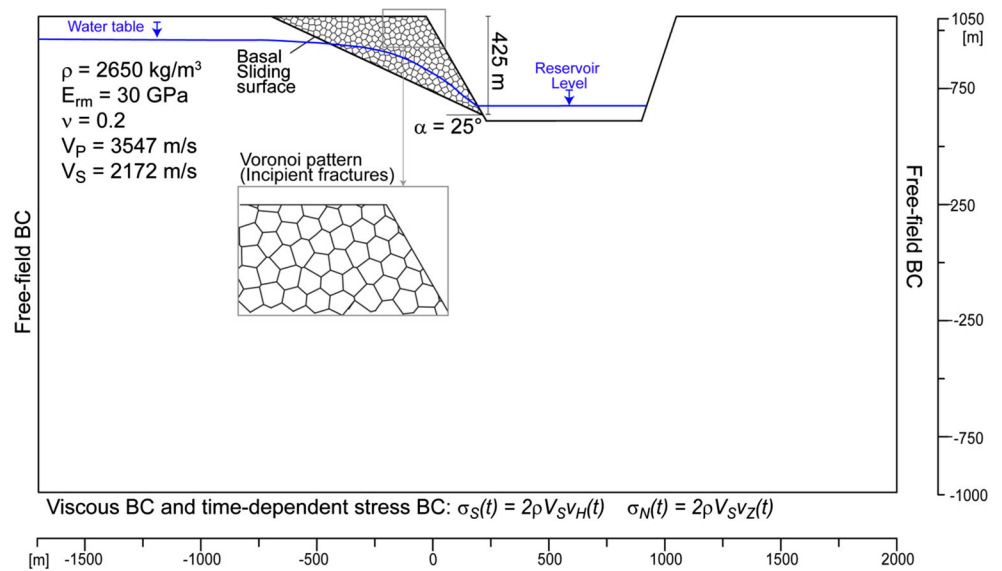**Fig. 6** Model geometry, boundary conditions and material properties (symbols and values also given in Table 1)

Table 1 Elastic and strength properties of the slope rock mass shown in Fig. 6

Rock mass	
Density, ρ [kg/m^3]	2650
Young's modulus, E [GPa]	30
Poisson's ratio, v [−]	0.2
P-wave velocity, V_P [m/s]	3547
S-wave velocity, V_S [m/s]	2172
Sliding surface	
Friction angle, ϕ [°]	32
Cohesion, c [MPa]	5
Tensile strength, T [MPa]	0.5
Residual cohesion, c_r [MPa]	0.5
Residual tensile strength, T_r [MPa]	0.05
Fracture normal stiffness, k_n [GPa/m]	1e10
Fracture shear stiffness, k_s [GPa/m]	5e9
Sliding mass (Voronoi contacts)	
Friction angle, ϕ [°]	40
Cohesion, c [MPa]	15
Tensile strength, T [MPa]	1.5
Residual cohesion, c_r [MPa]	0
Residual tensile strength, T_r [MPa]	0
Fracture normal stiffness, k_n [GPa/m]	1e10
Fracture normal stiffness, k_s [GPa/m]	5e9

1. The slope topography consists of a face dipping at 60°, which is representative of the steep rock slope profiles of the Matter valley and southern Swiss Alps (Fig. 5). The profile behind the slope crest is flat, which is favorable for limiting boundary effects during wave propagation.

2. A planar basal sliding surface dipping 25° out-of-plane is introduced to facilitate a kinematically simple failure mode. Coulomb strength properties are assigned to this surface that result in a stable slope configuration under gravitational loading. Note that assigning a cohesive (and tensile) strength may be interpreted as representing a partly developed sliding surface along which rock bridges and strong asperities have yet to be fractured. The sliding surface is comparable to the 30° dipping sliding surface responsible for the 1991 Randa rockslides.

3. A Voronoi fracture pattern dissects the rock mass above the sliding surface. The fractures represent a network of incipient fractures with lengths of approximately 25 m along which brittle fracture is simulated. The orientations of the fractures defining these polygons are random and do not group in predefined fracture families. The use of Voronoi networks is a common strategy to partly overcome the limitation of UDEC that only allows dislocations to occur along predefined and connected block contacts (Lorig and Cundall 1987). Sufficiently small Voronoi polygons provide the necessary degrees of freedom to simulate brittle fracture through contacts assigned equivalent intact rock strength properties (see Christianson et al. 2006; Martin et al. 2011; Gao and Stead 2014). Strength properties for the sliding surface and the Voronoi contacts are reported in Table 1. The Voronoi contact strengths were selected to represent the massive granitic and gneissic rocks encountered in the Matter Valley. The combination of a sliding surface with cohesive contacts that mimic intact rock bridges and a slide mass through which internal fracturing can be simulated to reduce internal kinematic constraints is ideal for modeling a rock collapse failure mode. Hungr et al. (2014) describe rock collapse as sliding occurring along an irregular rupture surface consisting of a

number of randomly oriented joints separated by segments of intact rock ("rock bridges"). This is commonly observed in strong rocks with non-systematic structure. The collapse failure mode is typified by the Randa 1991 failures as discussed by Hungr et al. (2014), and can also be ascribed to other catastrophic slope failure events in the region, including the previously described Medji rock collapse, 6 km north of Randa (Ladner et al. 2004; Jörg 2008).

4. A storage reservoir was placed adjacent to the slope and was connected to a generic groundwater table. Although not specific to the cases mentioned so far (Walkerschmatt, Plattja, Randa, Medji), steep mountain slopes bordering hydroelectric reservoirs, for example Checkerboard creek on the Revelstoke dam reservoir in British Columbia, Canada (Watson et al. 2007), represent scenarios with strong hydro-mechanical loading cycles exerted on the slope. Other examples of deep-seated landslides adjacent to hydroelectric reservoirs include the Hochmais-Atemkopf landslide in Austria (Zangerl et al. 2010), Little Chief landslide in British Columbia, Canada (Watson et al. 2007), and the Clyde, No. 5 Creek, Nine Mile Creek and Brewery Creek slides in New Zealand (Macfarlane and Gillon 1996). These hydro-mechanical conditions may be more adverse than simple groundwater fluctuations within most natural slopes, but they were chosen to: (1) compare enhanced hydro-mechanical effects to earthquake effects, and (2) to produce accelerated hydro-mechanical fatigue effects within reasonable computing times.

5. The elastic properties of the rock blocks correspond to crystalline rock with limited fracturing. A rock mass elastic modulus of 30 GPa was assumed (P-wave velocity of 3547 m/s), based on an intact rock modulus of 70 GPa and a GSI of 50–60 (using Hoek and Diederichs 2006). The values are in close agreement with elastic and seismic properties found in geophysical and laboratory investigations at the Randa slope (Willenberg 2004; Heincke et al. 2006).

2.3 Wave Propagation

For accurate modeling of wave propagation including damping due to frictional energy loss, UDEC includes a Rayleigh damping scheme (Itasca 2011). This is generally frequency-dependent, but can be assumed to be approximately frequency-independent around a center frequency f_{min}. Hence, for dynamic analyses the Rayleigh damping scheme must be chosen to be realistic in the frequency range of interest. Two parameters govern damping in the model, the center frequency f_{min}, and damping factor ξ_{min};

f_{min} is the frequency at which damping is minimal, while ξ_{min} is the fraction of critical damping. As seismic wave attenuation in crystalline rock is typically low (Bradley and Fort 1966), we choose low damping in the frequency range of interest in our models. Real earthquake ground motions as used in our models (see Sect. 2.5) contain dominant energy at frequencies between 0.5 and 5 Hz. Hence, following the guidelines of Itasca (2011), ξ_{min} was set to a small value, 0.005 in our case, while f_{min} was set to 2 Hz, meaning that damping was minimal between 1 and 4 Hz, but also reasonably small for our purposes between 0.5 and 8 Hz. Another key consideration for accurate wave representation is ensuring sufficiently fine discretization to avoid adverse effects—such as aliasing—in the frequency range of interest. We follow the recommendations of Kuhlemeyer and Lysmer (1973) and chose a minimum mesh size smaller than 1/10–1/8 of the minimum wavelength (i.e., of the highest frequency) in the model. In our study, the lowest seismic velocity is $V_s = 2172$ m/s. Hence, a maximum mesh size of 20 m can accurately represent wave lengths of minimum ~ 200 m, corresponding to frequencies of 10 Hz. Additionally, input ground motions were low-pass filtered to suppress frequencies above 10 Hz.

Adverse boundary effects, such as reflections at the side and bottom of our model, were avoided by using absorbing boundary conditions. Free-field boundary conditions at the side boundaries simulate an infinite continuum. At the base of the model, viscous boundary conditions (i.e., dash pots in the normal and shear direction) are used. These require that basal input motions be converted into stress boundary conditions, calculated as:

$$\begin{aligned} \sigma_n(t) &= 2\rho V_P v_n(t) \\ \sigma_s(t) &= 2\rho V_S v_s(t) \end{aligned}, \tag{1}$$

where σ_n and σ_s are the time-dependent normal and shear stresses at the bottom boundary, V_P and V_S are P- and S-wave velocities, respectively, v_n and v_s are the instantaneous vertical and horizontal velocity input motions, and ρ is the rock density (Itasca 2011).

2.4 Stress Initiation

Before performing dynamic analyses, an in situ stress state was initialized in our model. For this, we assigned stress boundary conditions to the sides and let the model equilibrate to gravitational loading. The stress boundary conditions assume lithostatic stress with equal horizontal and vertical stress and zero shear stress, (i.e., $\sigma_{xx} = \sigma_{zz} = -\rho g \Delta z$, $\sigma_{xz} = 0$, where Δz is the vertical distance from the top boundary at the sides and g is the gravitational acceleration). For the out-of-plane stresses, the plain-strain assumption is used. During the earthquake sequences, the

model was run to reach a new equilibrium state after each seismic event. A water table was initiated in the model before the seismic analysis (blue line in Fig. 6). Below the water table level, the pore pressure p increases under hydrostatic conditions: $p = \rho_w g \Delta h$, where ρ_w is the water density and Δh indicates the water column. This condition is representative of a groundwater system within the rock slope intersecting the ground surface at its toe. Moreover, a hydrostatic stress boundary condition is applied to the boundary nodes located along the valley bottom (see reservoir level line in Fig. 6), to simulate the presence of the storage reservoir at the toe of the slope.

2.5 Earthquake Sequences

To study the effect of repeated seismic loading, we applied sequences of real earthquake ground motions as bottom boundary conditions (Fig. 7). These were taken from the database of the seismic slope stability software package SLAMMER (provided by the USGS; Jibson et al. 2013). To obtain a number of earthquakes representative of a tectonic sequence, we randomly drew events with magnitudes conforming to the Gutenberg–Richter distribution $\log_{10}(N \geq M_i) = a - b \times M_i$ (N is the number of earthquakes with magnitude larger than M_i, a and b are constants). We chose a value for $b = 1.0$ (Fig. 7), which can be considered a global average (Schorlemmer et al. 2005). A total of 15–20 events were selected with a minimum magnitude chosen to be M5.7. Ideally, realistic input ground motions at the model bottom boundary would entail real records that are not or only marginally affected by local site effects by sediment layers with low seismic velocity. Thus, we chose only recordings from site classifications A or B (A: Rock, $V_s > 600$ m/s or <5 m of soil over rock; B: shallow stiff soil less than 20 m thick overlying rock). Epicentral distance of the used recordings was limited to <100 km.

Fig. 7 Acceleration ground motion used as bottom boundary condition (after translating into a velocity ground motion) as taken from the database provided with the software package SLAMMER (Jibson et al. 2013). The events were randomly chosen such that the magnitudes loosely follow a Gutenberg–Richter frequency magnitude distribution (b value $b \approx 1.0$). Also indicated are the epicenter distance D_e and the peak ground acceleration PGA. Only ground motion recordings from site classes A and B (see text) were chosen
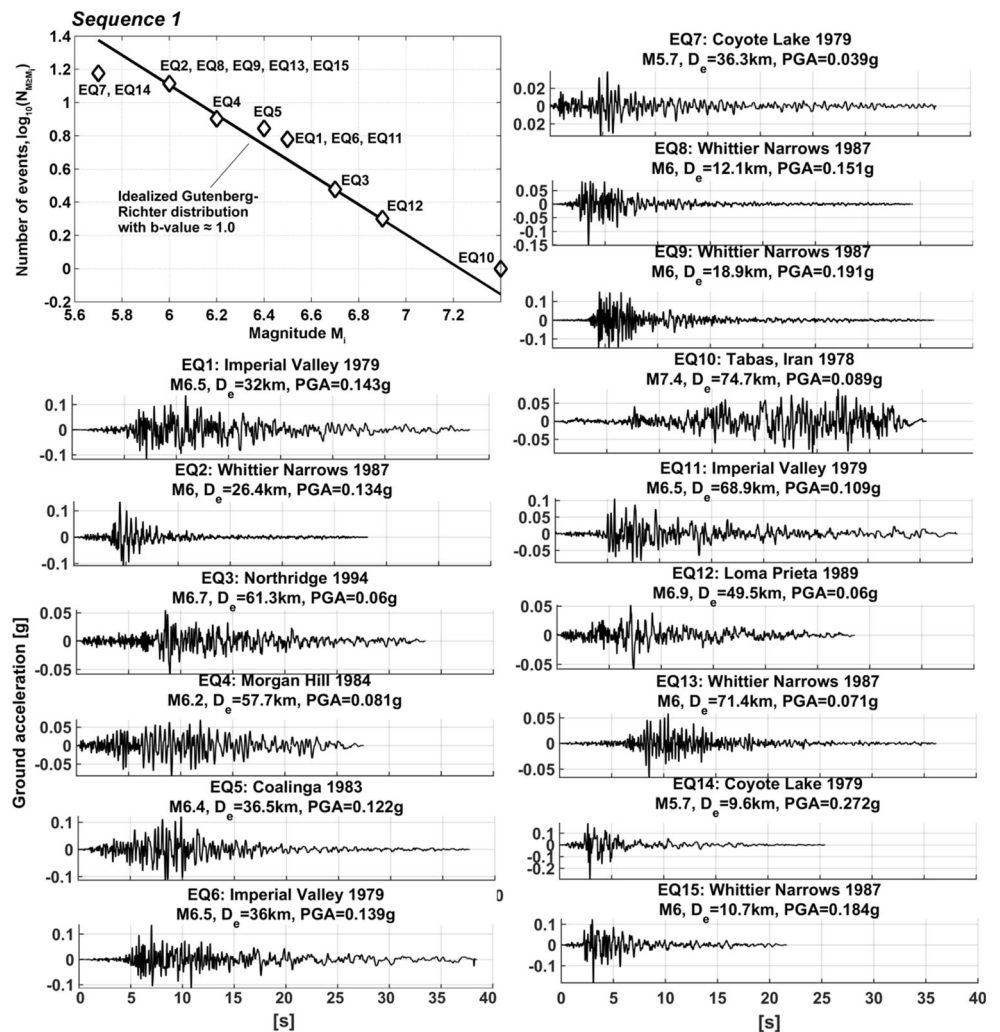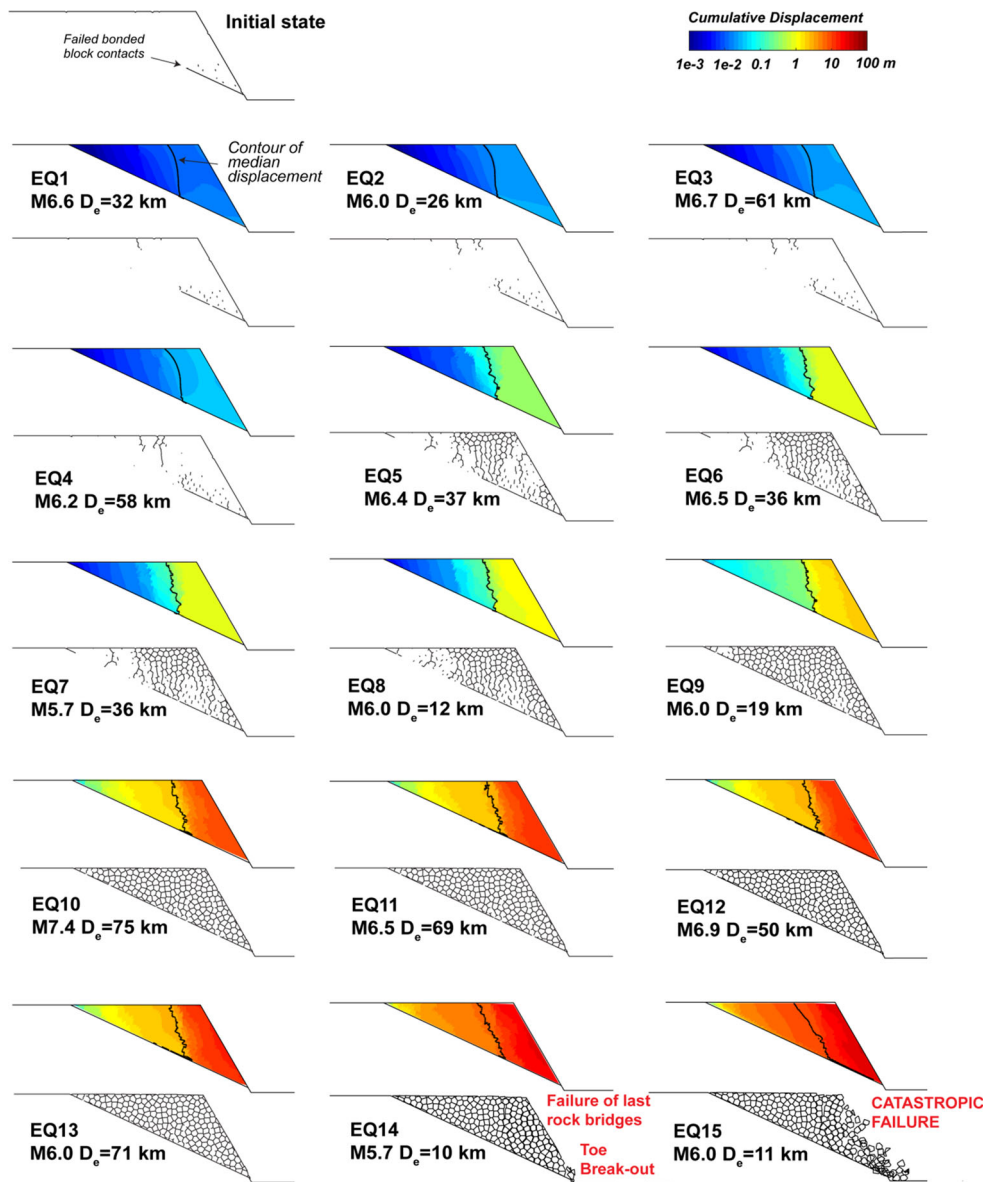
Fig. 8 Displacements fields
and failed discontinuities (failed
bonded block contacts) after
each earthquake in the sequence
shown in Fig. 7. The *thick black
line* is the median value of the
displacement within the sliding
body. Catastrophic failure
occurs after the 15th earthquake
(EQ15)

3 Seismic Fatigue

The cumulative rock mass displacement field as well as the
patterns of failed block contacts induced by each earth-
quake in the sequence of Fig. 7 is presented in Fig. 8. The
median displacement within the slope is marked as a black
contour on the displacement field. The maximum dis-
placement occurs at the toe of the sliding body. Figure 9a
shows the cumulative displacement within the sliding body
as a function of the number of earthquakes (median as a
black line, range between maximum and minimum as gray
shading). Note that the scale is logarithmic (as is the color
scale in Fig. 8); the near-linear increase actually implies an
exponential increase of cumulative displacement with each
successive earthquake event. The displacements within the
slope span several orders of magnitude indicating

substantial internal damage and dilation. Damage within
the sliding body is quantified as the percentage of contacts
that have failed relative to all contacts in the model (i.e.,
Voronoi contacts and those along the sliding surface;
Fig. 9b). Contacts that have failed in tension, i.e., open
fractures, are shown separately. Due to extensive extensile
failure and hence fracture opening, the rock mass of the
sliding body dilates. Evolution of volumetric dilation is
quantified as change in volume $V_0 - V_{EQ}$ due to earth-
quakes relative to the initial sliding block volume V_0, and is
shown in Fig. 9c.

The first earthquake in the series induces a maximum
displacement of about 20 mm (Fig. 9a). With each subse-
quent earthquake, the cumulative displacement increases
until collapse of the slope occurs with EQ15 (i.e., catas-
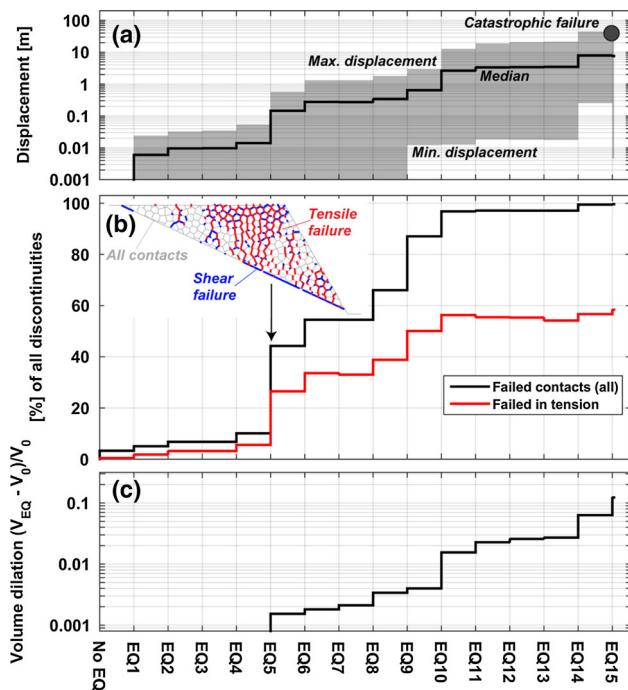trophic failure). In our numerical experiment, catastrophic

Fig. 9 **a** Displacement induced by the earthquake sequence in Fig. 7. *Black line* is the median (*black contour* in Fig. 8), *gray shading* represents the range of minimum to maximum displacement within the sliding body. **b** Damage induced by the earthquake sequence represented as the percentage of bonded block contacts ('incipient fractures') that have failed of all bonded block contacts. *Black* represents the contacts that have failed either in shear or tension, *red* represents those that have failed in tension (i.e., that are open). **c** Volumetric dilation after each earthquake, which is the change in sliding block volume ($V_{EQ} - V_0$) with respect to the initial volume V_0 (color figure online)

failure is detected when the model is unable to reach static equilibrium; the failure mode is interpreted based on visual indicators. A first major step in displacement (Fig. 9a), in response to rock slope damage (i.e. failed contacts; Fig. 9b) and dilation (Fig. 9c), occurs after EQ5. About 0.7 m of additional displacement occurs after this earthquake and for each of the next six earthquakes that follow (Fig. 9a). Before this, displacements are only in the range of 0.01 m per event and the brittle fracture damage is limited to the localization of the sliding surface and opening of tension cracks behind the slope crest. Volumetric dilation is negligible before EQ5 (Fig. 9c). With EQ5 almost 50 % of all contacts have failed (Fig. 9b). Fracturing then continues until after EQ10 when almost 100 % of all contacts have failed and are at their residual strength. Between EQ5 and EQ10, dilation increases from 0.2 % to about 0.4 % (Fig. 9c). EQ10 (M7.4) induces about 10 m of displacement and thus doubles the displacement induced by the nine preceding earthquakes. Volumetric dilation increases to about 1.5 %, and almost all contacts have failed. Afterwards, additional displacements only occur during

EQ11 and EQ14 (Fig. 9a). Interestingly, failure of almost all contacts, reducing the slope to a highly disturbed, fragmented mass at residual strength (Fig. 8), is not sufficient to bring the slope to collapse. Further dilation from 1.5 % (EQ10) to 7 % (EQ14) is required (Fig. 9c). Substantial block mobilization occurs after EQ14, during which five blocks at the toe break-out and the few remaining intact rock bridges rupture (Fig. 8). However, the accelerating slope movements eventually decelerate (i.e., the model can still reach static equilibrium), and catastrophic collapse does not occur until the next earthquake (EQ15) suggesting that with toe break-out the slope reaches a critical level of fatigue (Fig. 8). At this point, the slide body has experienced sufficient internal shearing, dilation and rotation of key blocks to provide the necessary kinematic freedom for catastrophic release. Prior to EQ15, up to 40 m of maximum displacement (8 m median displacement) and 7 % of dilation had occurred (Fig. 9).

4 Sensitivity to Kinematics, Earthquake Sequence and Strength

Assumptions regarding the geometrical features of the slope, i.e., the 60° steep slope face, the 25° sliding surface, and the Voronoi pattern of incipient fractures, are recognized as having a major influence on the modeled kinematic behavior. A comprehensive sensitivity analysis focusing on slope kinematics goes beyond the scope of this study, although we are well aware that kinematics has an impact on the response to cyclic load changes (e.g., Gischig et al. 2011b). Accordingly, we applied the earthquake sequence in Fig. 7 to three additional slope configurations (Fig. 10). We reduced the slope face angle from 60° to 40° in geometry 2 (geometry 1 is the initial geometry in Fig. 8), reduced the dip angle of the sliding surface from 25° to 10° (geometry 3), and replaced the Voronoi fracture network by two near-orthogonal fracture sets (geometry 4).

In geometry 2, displacements as well as damage increase slowly up to EQ9 (relative to that for geometry 1). During EQ9 displacements increase to almost 1 m, damage to about 90 %, and dilation to 0.7 %. Interestingly, after EQ9, the displacement curves of geometry 1 and geometry 2 are nearly identical. Almost all contacts have failed and displacement is controlled by the mobilization of the block assembly along the sliding plane. After this point, the overall displacement behavior becomes very similar. With respect to the collapse mechanism, the lower slope face angle in geometry 2 accommodates more deformation; in contrast, the steeper slope face of geometry 1 collapses with lower displacements.

Displacements and damage for the case of geometry 3 are generally lower because the sliding plane is dipping at
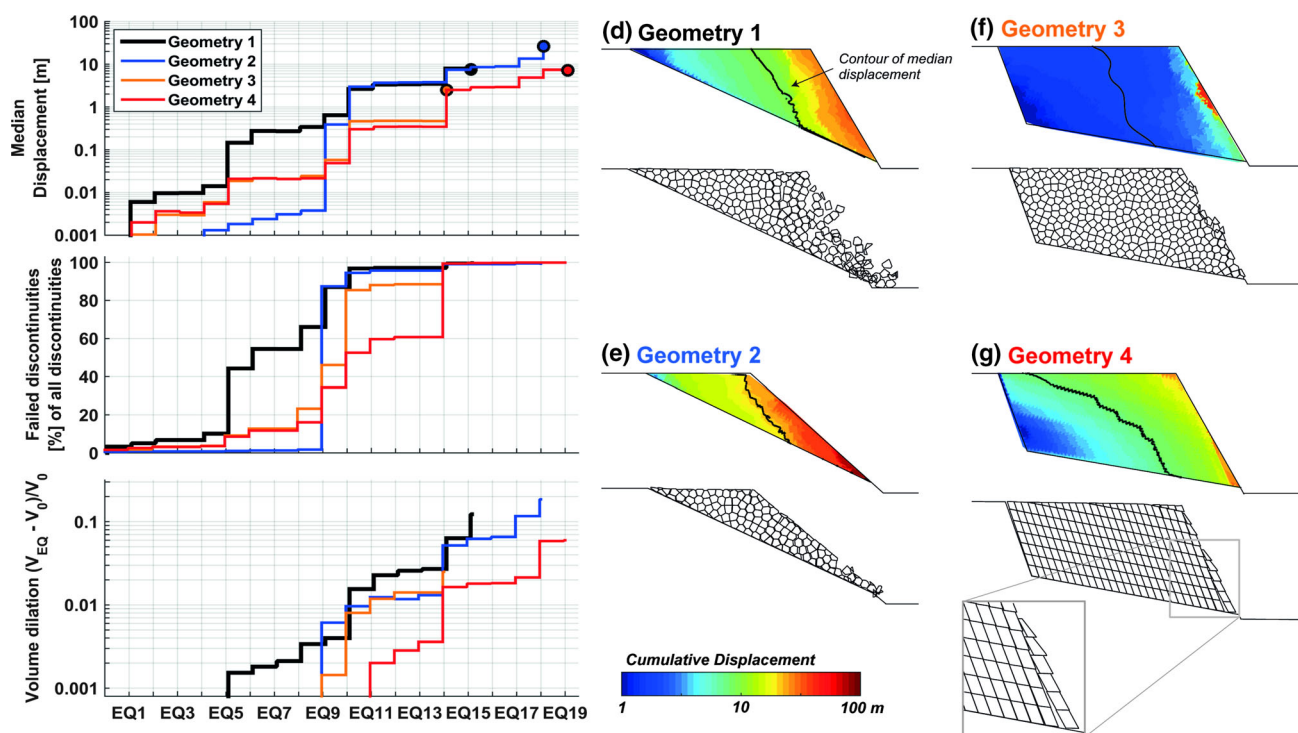
Fig. 10 a Median displacement as in Fig. 9a for different slope geometries (geometry 1–4). **b** Seismically induced damage (i.e., percentage of failed block contacts) as in Fig. 9b for the different slope geometries. **c** Volumetric dilation (as Fig. 9c). **d**–

g Displacement field of the four geometries (*top*) and blocks assembly during catastrophic failure (i.e., when the model could not be run to equilibrium anymore (*bottom*)

only 10° (in contrast to 25° for geometry 1). The largest displacements occur at the slope face. Despite smaller displacements, ultimate failure and collapse occur earlier than for geometry 1 once blocks at the slope face mobilize. Hence, for geometry 3 the failed volume is smaller and limited to a smaller portion of the rock mass due to kinematic constraints, while for geometry 1 almost the entire sliding mass is involved in the collapse.

Similarly, the displacements for geometry 4 are lower than for geometry 1, again because of the flatter basal sliding surface. Compared to geometry 3, however, the entire rock mass is deforming because sliding is facilitated by the multiple discontinuities dipping out of the slope. The non-systematic orientation of the Voronoi contacts provides a degree of block interlocking. Maximum displacements occur at the slope toe and crest. Catastrophic failure and collapse occur as soon as the block column at the toe defined by the sub-vertical fractures start slumping (see Fig. 10g; inset figure for geometry 4). Similar to geometry 3, only a small portion of the rock mass is mobilized during catastrophic failure.

Overall, Fig. 10 illustrates that kinematics play a major role in the failure mode and failure volume by influencing the evolving slope response to each earthquake loading cycle. Similar observations were made for thermo-elastic

load changes in slopes by Gischig et al. (2011a), who found that thermo-elastic effects differed in their efficiency and pervasiveness in promoting toppling or sliding kinematics. At the same time, the evolution of co-seismic damage and deformation for the different cases tested do show a consistent pattern that, regardless of structural settings, the state of damage and slope displacements become more and more critical with each earthquake event.

To assess the potential variability of our results due to the randomly chosen sequence, we compute displacements and damage for four additional earthquake sequences randomly drawn from the sample population using the same strategy described in Sect. 2.5. Hence, each of these additional sequences contain earthquakes with magnitudes ranging from M5.7 to M7.4, with epicenter distances less than 100 km, and with peak ground acceleration (PGA) values of 0.04–0.33 g.

The results indicate that the displacements and damage evolution are comparable for all sequences (Fig. 11a); more than 95 % of discontinuities have failed after 8–12 earthquakes, and catastrophic failure occurs after 14–16 earthquakes. Similar to the reference case in Fig. 9 (corresponding to sequence 1 in Fig. 11a, b), sequences 2 and 4 both experience toe break-out followed by catastrophic failure during the next earthquake. In sequence 3, toe
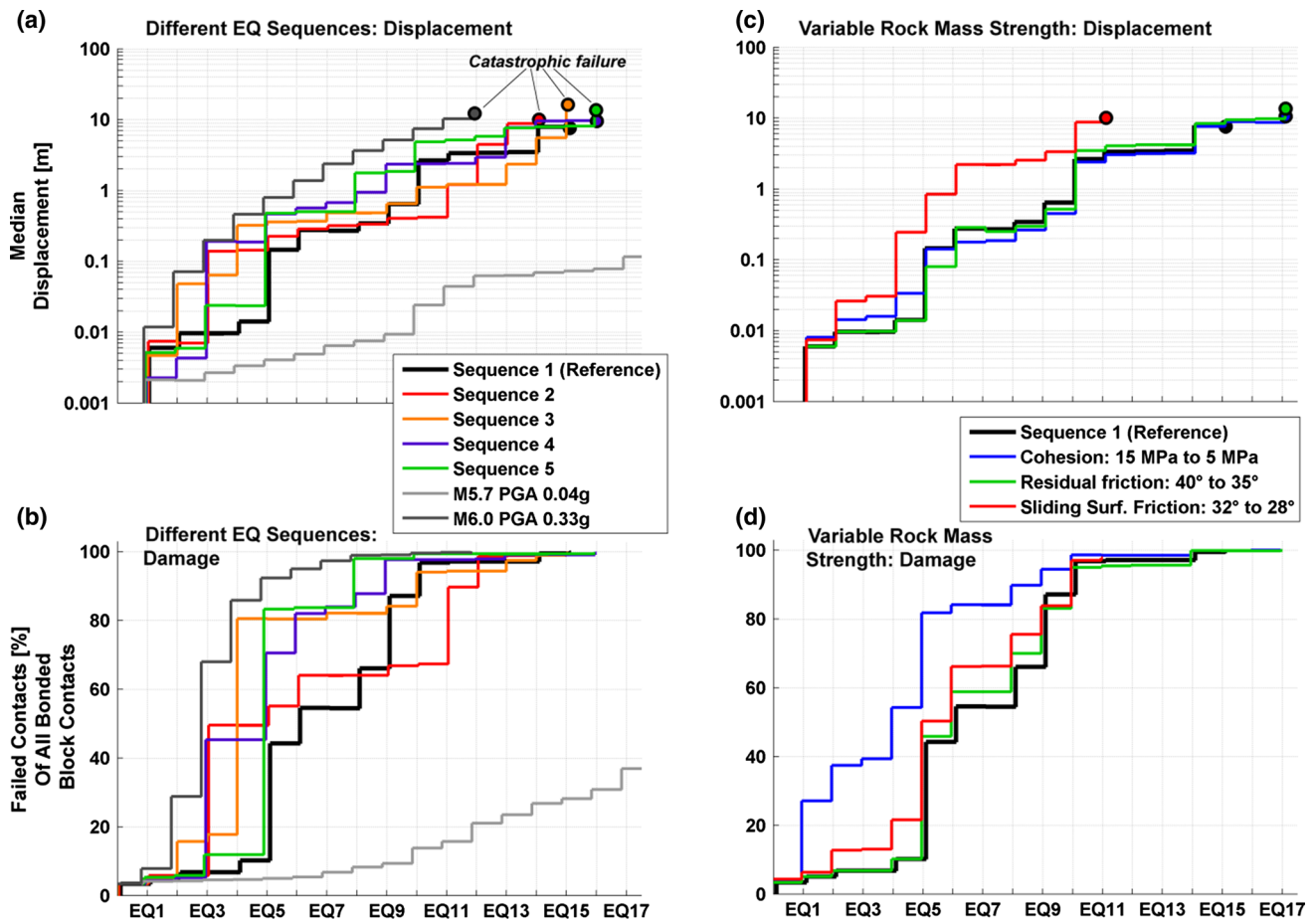
Fig. 11 a Sensitivity of seismically induced displacement (only median shown as in Fig. 9a) to the sequence, i.e., the randomly chosen earthquakes in different sequences (the reference sequence is the one shown in Fig. 7). The last two sequences only consist of a single earthquake each, i.e., a M5.7 and an M6.0 earthquake. **b** Damage represented as the percentage of bonded block contacts that have failed of all bonded block contacts. **c, d** same as **a, b** focussing on sensitivity to different strength properties

break-out and catastrophic failure occur during the same earthquake (EQ15). In contrast, toe break-out in sequence 5 occurred during EQ13 and required three more earthquakes to trigger catastrophic failure. Note that in Fig. 11a only the median displacement is shown for clarity. Median displacement before catastrophic failure ranges between 5 and 10 m; the maximum displacements vary from 20 m (sequence 3) to 80 m (sequence 4).

Also shown in Fig. 11a, b are two sequences that consist of only one earthquake that is repeated several times. The repeated earthquakes represent the two extremes (upper and lower bound) in terms of PGA = 0.33 and 0.04 g as used in sequences 1–5, respectively. The earthquake with the largest PGA = 0.33 g leads to catastrophic failure after 12 repetitions. For the case with the lowest PGA = 0.04 g, catastrophic failure did not occur even after 24 repetitions (the computation was stopped due to memory and computation time limits). The two cases show that earthquake-induced displacement (and thus the probability for

catastrophic failure) depends on the strength of the earthquake. PGA and other characteristics of ground motions (e.g., Arias intensity) are often used to assess seismic slope stability (e.g., Jibson 2007, and references therein). However, the fatigue sequences also show that the impact of a certain earthquake does not only depend on its strength (e.g., expressed by PGA), but also on the loading history and pre-existing rock mass damage induced in the slope. The induced additional damage depends on how much previous damage the slope has incurred. For instance, in each case the incremental damage added during each repetition initially increases sharply; however, once more than 70–80 % of the bonded block contacts have failed, the incremental damage increases at a significantly lower rate for subsequent repetitions.

The sensitivity of the results to rock mass strength properties is explored in Fig. 11c, d for sequence 1. Here, only the parameters indicated in the legend were changed, while all other parameters were kept constant. Reducing

the rock mass cohesion (and tensile strength) to one-third of that used for the reference case resulted in damage initially accumulating faster during the first five earthquakes. However, the 100 % damage condition was reached at approximately the same time (EQ10; see Fig. 11d). The corresponding displacement trends were approximately the same with catastrophic failure occurring after EQ17 instead of EQ15 for the reference case. Lowering residual friction similarly does not have a strong effect on damage and displacement accumulation. However, decreasing friction of the basal sliding surface results in a somewhat faster accumulation of damage and a significantly increased displacement rate per earthquake. In this case, catastrophic failure occurs much earlier, i.e., after EQ10. Note that for all four cases, the median displacement before catastrophic failure was about 10 m. The result implies that for the investigated slope (geometry 1) there is a limiting displacement, and hence internal deformation, that has to be exceeded for catastrophic failure to occur. Within the range that bonded block contact properties were changed in Fig. 11c, d, this limiting displacement remained unaffected. Internal strength did not affect how fast the limiting displacement was reached. In our models, the sliding surface shear strength was the most sensitive parameter with respect to how quickly the limiting displacement is reached. The results confirm that catastrophic failure for the presented slope kinematics (translational sliding) does not occur even if significant damage is imposed changing the slide mass from a cohesive body to a frictional one

(Figs. 9c, 10b, 11b, d). Substantial additional dilation is required so that the kinematic release of blocks becomes possible through toe break-out and shear mobilization (Figs. 9c, 10c). For this, a minimum displacement and hence internal deformation must first be reached (Figs. 9a, 10a, 11a, c).

5 Dependence on Pre-existing Damage

The sensitivity analysis performed, although limited, demonstrates that a slope's response to earthquake loading will depend on its pre-existing damage state, and hence on the loading history. This observation is also demonstrated in Fig. 12. Three earthquakes were applied to the slope after each earthquake of sequence 1 (Fig. 7). The incremental additional displacement (median, maximum and minimum) induced by these three earthquakes are shown in Fig. 12. The curves show that the displacement induced by the same earthquake can vary by more than two orders of magnitude depending on pre-existing damage. First, the M6.7 earthquake (PGA = 0.36) induces 10–20 cm of displacement if applied to the slope before the start of sequence 1; i.e., before the slope has experienced any damage. If applied after eight preloading earthquakes (EQ8) based on sequence 1, almost 10 m of displacement is induced. As a result, catastrophic failure is triggered after EQ10 in sequence 1 when followed by the M6.7 earthquake. Recall that catastrophic failure occurred after EQ15

Fig. 12 Displacement (median as *thick line* and range between minimum and maximum) induced by three difference earthquakes as a function of pre-existing damage in the rock slope. Indicated on the *horizontal axis* is the number of earthquakes that have damaged the rock slope before. The preloading earthquakes correspond to those in sequence 1 in Fig. 7 (e.g., 10 preloading earthquakes correspond to earthquakes EQ1 to EQ10 of sequence 1)
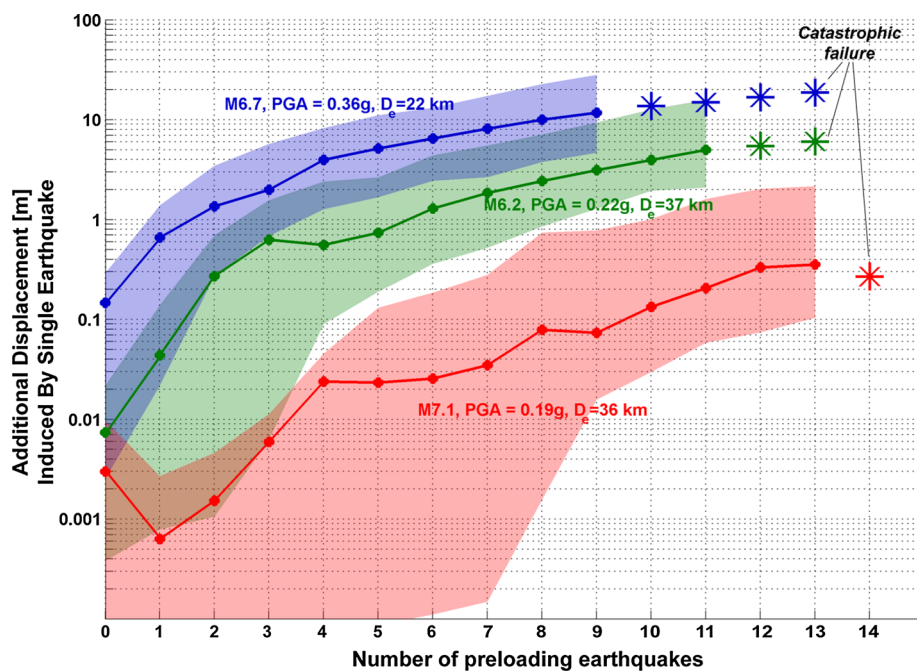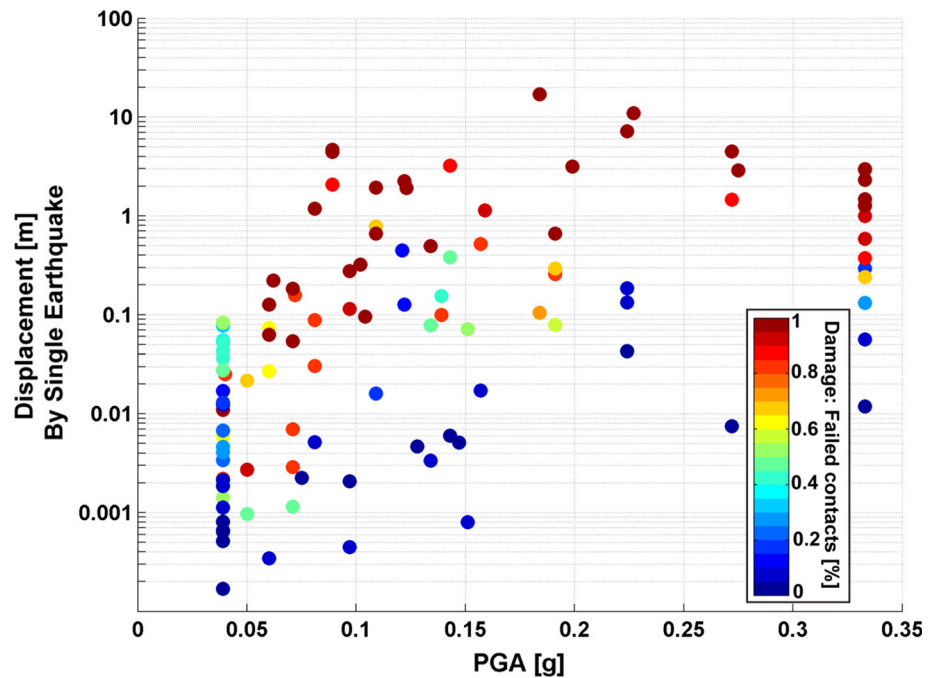
Fig. 13 Incremental displacement induced by single earthquakes as a function of PGA of the earthquake (*x*-axis) and pre-existing damage in the slope (*color code* representing percentage of failed contacts as in Figs. 9b, 11b, d). The displacement and damage values were taken from the sequences shown in Fig. 11a. Note, however, that displacements represent those induced only by the earthquake corresponding to the shown PGA, i.e., it is the incremental displacement, not the accumulated displacement up to the earthquake in the sequence

when following sequence 1 without the M6.7 earthquake. In Fig. 13, the incremental displacements (median) induced by each individual earthquake for all sequences in Fig. 11a are shown as a function of both PGA and pre-existing damage. The effect of PGA on displacement spans two orders of magnitude as can be well observed for the cases with little pre-existing damage (points with cold colors in Fig. 13). However, the amount of pre-existing damage has an effect on co-seismic displacement that can even exceed two orders of magnitude; the amount of damage and displacement that has accumulated before an earthquake largely determines how efficiently earthquakes induce slope deformations.

6 Interplay Between Seismic and Hydro-mechanical Fatigue

Repeated or cyclic loading of rock slopes can be driven by different mechanisms and several mechanisms can also act in parallel as illustrated in Fig. 1. We explore here the interplay between seismic and hydro-mechanical (HM) fatigue. Depending on the tectonic setting, the repeat frequency of a substantial earthquake (e.g., *M* > 6.0) can globally vary from a high of 0.5 damaging earthquakes per year for a seismically active region (e.g., close to an active tectonic boundary like the subduction zone in Japan), to less than 0.01 per year for a region with moderate seismic activity (e.g,. the southern Swiss Alps, Fig. 2). In the period between seismic events, the rock slope is also

affected by other cyclic loading mechanisms, such as the seasonal groundwater pressure variations due to rainfall and snowmelt periods or the raising and lowering of a water reservoir.

Hydro-mechanical fatigue was integrated in the earthquake fatigue model (Fig. 6) by applying: (1) cyclic groundwater pressure changes within the rock mass (i.e., by changing the ground water table), together with (2) cyclic fluctuations in the reservoir level at the valley bottom (i.e., by changing isotropic hydrostatic stress boundary conditions). These cycles were applied after each earthquake of the sequence presented in Figs. 7 and 8. The peak-to-peak groundwater pressure change during each cycle is 1 MPa at the observation point shown in Fig. 14 corresponding to a water column change of about 100 m. In the reservoir lake, the peak-to-peak water pressure change is 0.4 MPa, i.e., 40 m of water column. The situation mimics hydro-mechanical loading cycles in deep-seated landslides located close to a hydroelectric dam reservoir, such as the Hochmais-Atemkopf landslide, Northern Tyrol, Austria (Zangerl et al. 2010) or the Little Chief landslide, British Columbia, Canada (Watson et al. 2007). As a comparison, observed pressure fluctuations in the Campo Vallemaggia landslide in Switzerland are 0.5 MPa (Bonzanigo et al. 2007; Preisig et al. 2015). The frequency of water pressure fluctuations matches 1 cycle per year. For simplicity the cycles are sinusoidal. We acknowledge that this may not be typical for the shape of pressure cycle fluctuations associated with snowmelt and/or rainfall events as well as reservoir level changes. Also
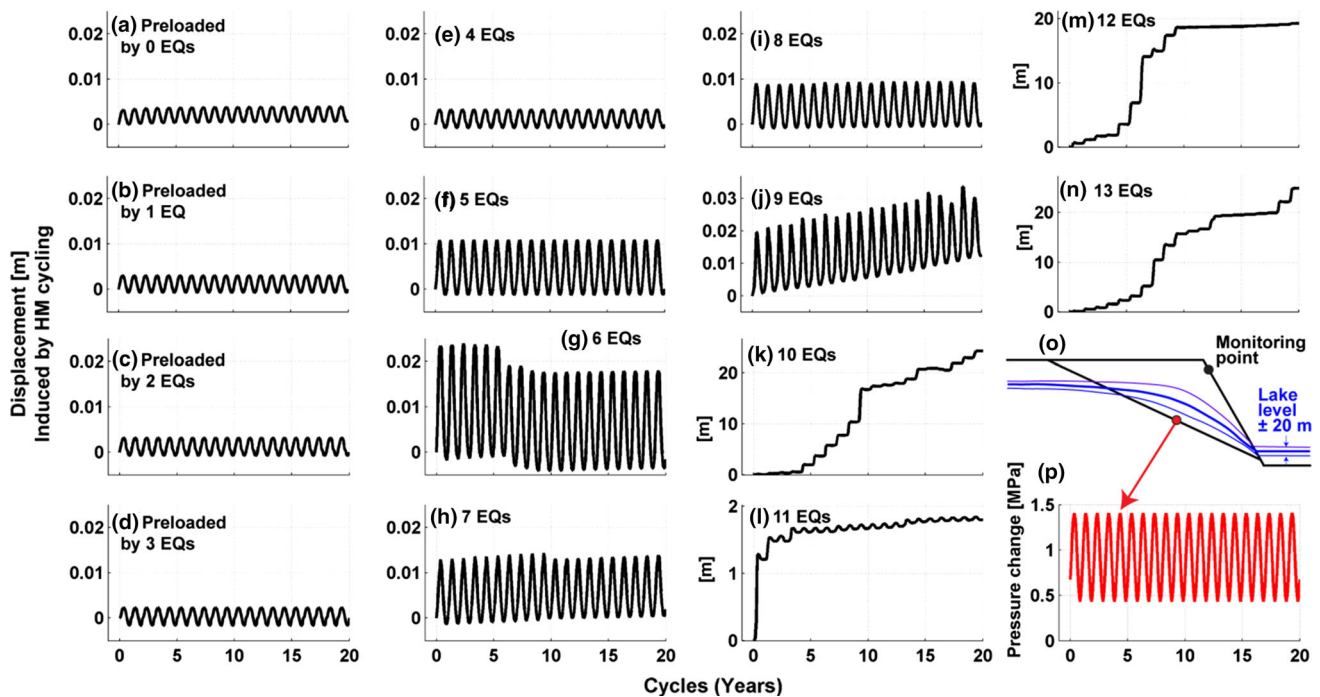
Fig. 14 **a–n** Displacements induced by 20 hydro-mechanical cycles as a function of damage induced by the indicated number of earthquakes. The earthquakes correspond to those in sequence 1 (Fig. 7). **o** Geometry of the ground water table and changes thereof. Displacement time series in **a–n** were taken from the indicated monitoring point. **p** Pressure time history at the *red point* indicated along the sliding surface in **o**) (color figure online)

the amplitude of the fluctuations may be rather high, but help to accentuate the effects of hydro-mechanical fatigue within reasonable computing times.

Figure 14 shows displacements at the indicated monitoring point induced by 20 water pressure cycles following each damage state presented in Fig. 8. At the initial state of the slope and up to earthquake EQ4, the hydro-mechanical cycles, although rather strong with a peak-to-peak amplitudes of up to 1 MPa, are not sufficient to induce additional permanent slope displacement and damage. Displacement time series show a cyclic signal with peak-to-peak amplitude of 3 mm, which arises from the compliant response of fractures. Similar, cyclic hydro-mechanically induced slope displacement have been observed in natural slopes (i.e., valley closure and opening of about 12 mm; Hansmann et al. 2012). The peak-to-peak amplitude of these displacement cycles increases to 10–20 mm after EQ5, during which substantial damage was induced (up to 50 % bonded block contacts failed). At this point, up to 30 % of the induced fractures are open; i.e., they are no longer in contact and are not transmitting stress. Hence, compliance of these discontinuities has increased, which leads to a substantial increase in the cyclic displacement amplitude. The dependence of reversible hydro-mechanically induced slope displacement has been discussed by Zangerl et al.

(2010). The HM-induced slope displacements here are not permanent up to EQ8. Only after EQ9 do the hydro-mechanical cycles generate permanent displacements; approximately 1 cm after 20 cycles. These increase to 2 cm after EQ10, when almost all bonded block contacts have failed and the impact of the hydro-mechanical cycles changes dramatically. Permanent displacements after 20 cycles reach 2 m after EQ11, and 20 m after EQ10, EQ12 and EQ13. After EQ14 the slope failed catastrophically during the first hydro-mechanical cycle. Interestingly, the HM-induced displacement time series are not uniform between these earthquakes, and they also do not increase linearly although each repeated cycle has the same amplitude. After EQ10 the displacement rate is small for the first 4 cycles. It then increases and exhibits a major step of a few meters during the 9th cycle. Such step-wise increases in slope deformation are characteristic for fatigue processes. Accumulation of deformation leads to local failure of contacts associated with stress redistribution, and as a consequence, to a phase of enhanced deformation response. Such temporary slope accelerations may not necessarily occur during a period of enhanced forcing (e.g., a heavy rain fall event), but can occur during a cycle that is similar in magnitude to previous ones that induced less deformation. A similar case has been described by

Bonzanigo et al. (2007), who report on different phases of enhanced deformation of the Campo Vallemaggia landslide in Switzerland, which are not directly related to exceptional water pressure increase.

Observations in Fig. 14 are in line with the damage-dependent seismically induced displacements reported in Figs. 12 and 13. These findings illustrate that the response of a rock slope to a loading event is indicative of the level of pre-existing damage or the degree of criticality of the rock slope. Larger displacements during an earthquake or high displacement rates due to ground water pressure changes indicate that the slope has experienced a history of substantial damage and thus is in a more critical state.

## 7 Assessing Damage and Fatigue—Damage-Dependent Spectral Amplification

As illustrated by the cases of Plattja and Walkerschmatt (Fig. 3b, c), wide open tension cracks are evidence of past periods of slope deformation and damage. However, these indicators are largely restricted to surface observations, presenting limited means for projecting how damaged a rock mass might be at depth. Displacement monitoring provides valuable insights into the temporal behavior of a landslide, with magnitudes, velocities and accelerating behavior serving as indicators of the criticality of a rock slope. However, given the short time window over which data are collected relative to that over which progressive failure develops, the data can sometimes be ambiguous

with acceleration episodes suggesting a critical state only to be followed by less alarming values; similarly, slopes not exhibiting large displacements may nevertheless be in a critical state and highly susceptible to a future seismic event. We argue in the following that seismic wave field characteristics (i.e., the seismic response) of an unstable rock mass may provide another indicator for past deformation and damage.

Recent observations of ambient seismic noise characteristics on unstable rock slopes have led to the emergence of a novel method to identify rock masses that have undergone substantial deformation in the past. Burjánek et al. (2010, 2012) showed for two instabilities in Southern Switzerland—the current Randa instability and the Walkerschmatt instability (Figs. 3c and 4a, respectively)—that seismic waves are strongly amplified and polarized within the unstable rock mass due to the presence of open tension cracks acting as compliant structures. Figure 15 presents the results by Burjánek et al. (2012) for the case of Walkerschmatt, with Fig. 15a showing the locations of the seismic stations that recorded ambient noise for 1–2 h. For three stations the spectral amplification with respect to a reference station are shown in Fig. 15b. For the three frequencies 1.6, 2.3 and 3.7 Hz, amplification maps are shown (Fig. 15c–e) that represent the spatial distribution of amplification. Amplification of waves with frequencies of 1.6 Hz increases towards the slope crest. For the higher two frequencies more heterogeneity behind the crest can be observed. The maximum amplification factors derived from ambient noise recordings reached 7 at a frequency of

Fig. 15 Observations of seismic wave amplification and polarization from ambient noise recordings at Walkerschmatt (see Burjánek et al. 2012 for details). **a** Map view and array of seismic stations deployed at the site during. **b** Spectral amplification of three stations indicated in **a** with respect to the reference station. **c** Wave amplification into the direction of maximum polarization (indicated by the *black arrow*) for frequencies of 1.6 Hz. **d**, **e** Same for 2.3 and 3.7 Hz, respectively
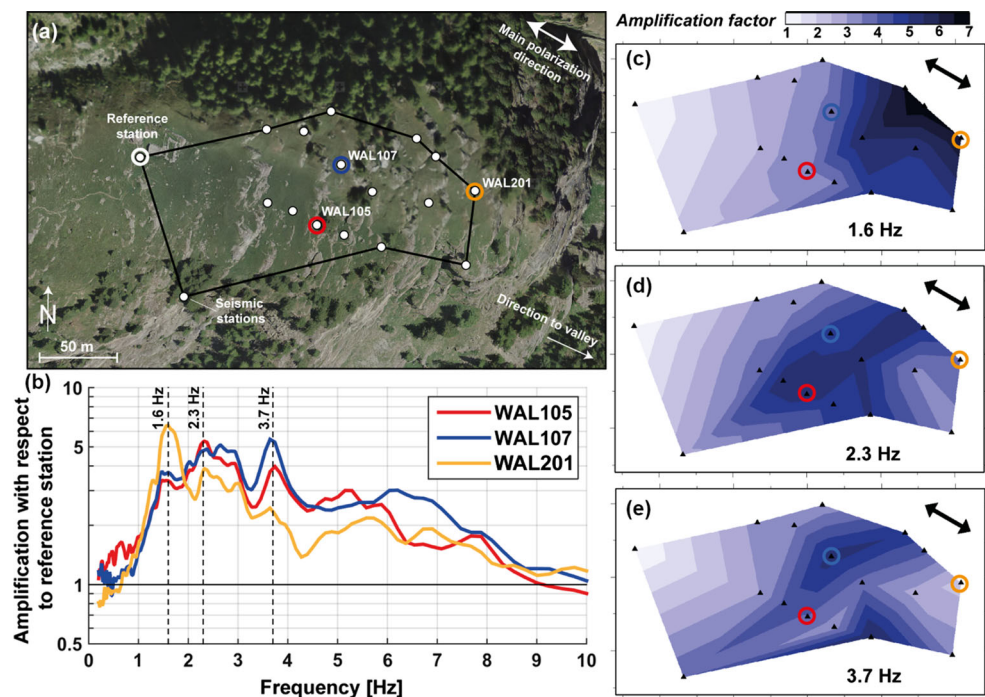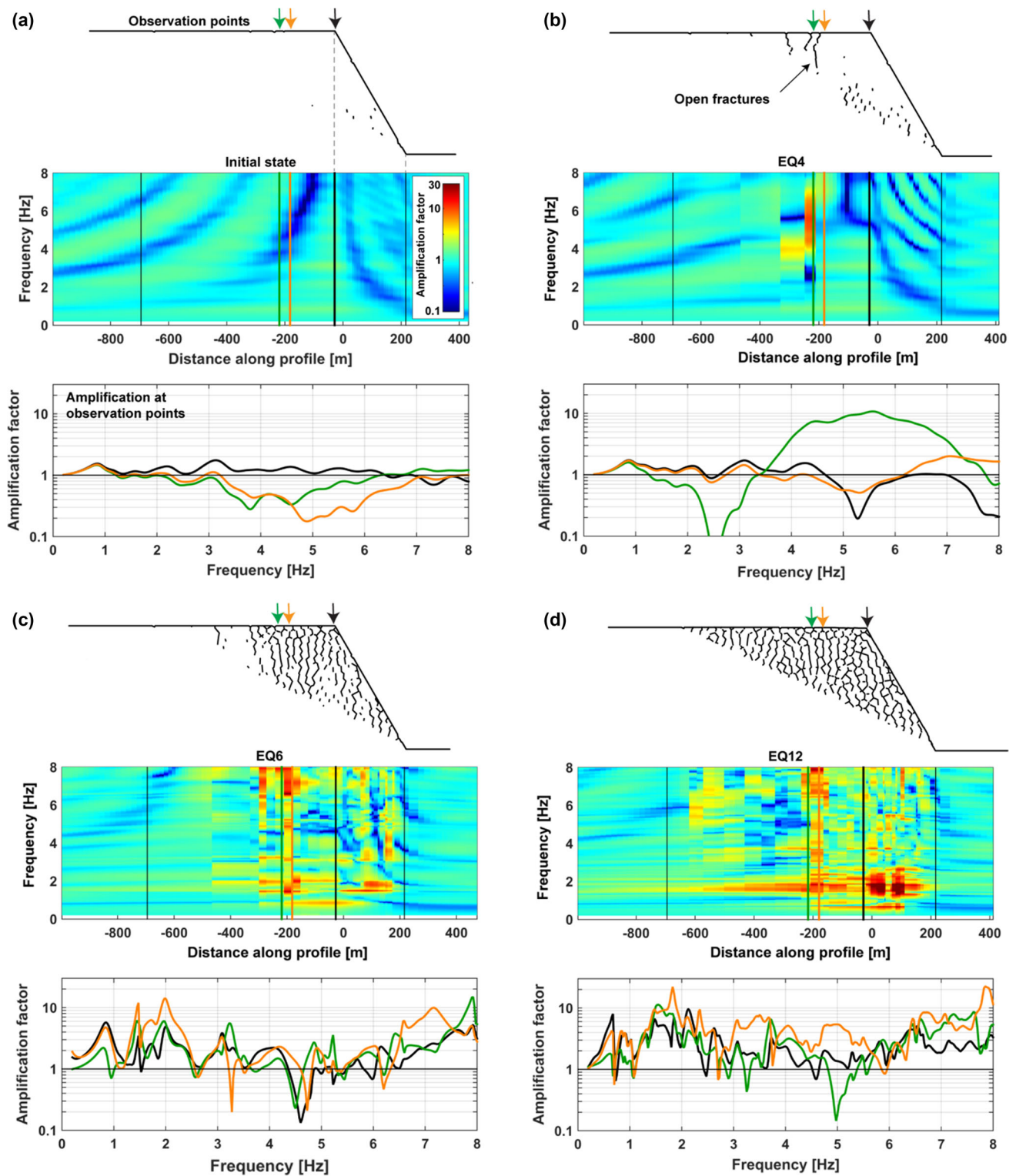
1.6 Hz. The waves of the ambient noise were polarized normal to the tension cracks and into the direction in which predominant rock mass movement is expected. It was interpreted that these phenomena arise from eigenmode vibration of the blocks. The amplification characteristics

are related to block dimensions between compliant tension cracks. At the Randa instability, amplification reached factors of 5 at 3 Hz and 7 at 5 Hz (Burjánek et al. 2010, 2012). For this case, it was possible to reproduce observed amplification characteristics using numerical modeling

◀ **Fig. 16** Seismic wave amplification as a function of both distance along profile and frequency. The topmost part of each subfigure shows the slope surface along with the fractures that have failed in tension (i.e., open fractures). The *color-scaled* map in the middle shows amplification patterns along the profile and as a function of frequency. Note that the distance scale of the amplification pattern is equivalent to that for the slope geometry above. The *thick black line* corresponds to the slope crest. Amplification is derived analogous to Gischig et al. (2015), and Bourdeau and Havenith (2008), i.e., it indicates how much ground motions propagating from the bottom boundary of the model to the surface are amplified at observation points at the surface. The bottom-most part of each subfigure shows spectral amplification at positions along the profiles indicated by *colored lines* in the amplification pattern and the *arrows* on the slope geometry. **a** Amplification characteristics of the initial state, i.e., without earthquake preloading. **b–d** Amplification characteristics after EQ4, EQ6, and EQ12, respectively

(i.e., UDEC) and consideration of deep and highly compliant tension cracks (Moore et al. 2011). Gischig et al. (2015) demonstrate that amplification characteristics are sensitive to changes in the damage state within the rock mass. At increasing internal deformation and damage, tension cracks behind the slope crest grow in number and depth, which causes changes in the surface amplification patterns.

For the slope at different stages of fatigue in Fig. 8, we compute amplification patterns as a function of both distance along profile and frequency as it may be observed at the surface (Fig. 8). The method for deriving these amplification patterns was adapted from Bourdeau and Havenith (2008), and was also used by Gischig et al. (2015) to explore amplification characteristics of different slope configurations. It is based on Ricker-wavelets used as input motions at the bottom boundary. Ricker wavelets are often used in amplification and eigenmode vibration studies. They are characterized by their short time duration and well-defined spectral content around a dominant frequency f_{dom} (e.g., Gischig et al. 2015). To be able to determine amplification patterns in a frequency range of 0.1–8 Hz, we used two different wavelets with $f_{dom} = 0.5$ and 4 Hz. From a densely spaced array of observations points at the ground surface of the model, we derived amplification as the ratio of the spectra of each observation point to the spectrum of the input Ricker wavelet (i.e., at the bottom boundary). The final spectral amplification curve at each observation point is an average of the amplification spectra for the two wavelets (0.5 and 4 Hz wavelet, see Gischig et al. 2015). The spectral amplification for all observation points at the ground surface is shown in Fig. 16 as color-coded maps with profile distance and frequency as axes. Note that in a homogeneous half-space, the spectral ratio of a wave traveling towards a free surface compared to the wave at the surface is two due to the free-surface effect (i.e., superposition of the incident and reflected waves doubling the amplitude at the surface). Thus, for

amplification curves computed at the surface, spectral ratios between observation points and the basal input motion were divided by two.

For four stages of damage and fatigue in Fig. 8, amplification patterns and spectral amplification curves for three locations behind the slope crest are presented in Fig. 16. Also shown are the slope profiles with fractures that have opened at each stage, and thus have become compliant structures. The initial state shows amplification characteristics of a largely undisturbed slope (Fig. 16a). Amplification factors reach values of less than 2 for frequencies of 0.8 and 3 Hz (note that the color scale is logarithmic). Once fractures open at the surface, amplification patterns become discontinuous and change across every tension crack (Fig. 16b). For a small block separated by two small tension cracks, an amplification factor of up to 10 occurs at frequencies around ∼6 Hz. Behind this block, a wider block is separated by a deeper tension crack to the back. For this block, amplification factors of 3–4 occur at around 4 Hz. After EQ6, fracturing becomes more intense (Fig. 16c). Many fractures are open, and the resulting amplification pattern becomes heterogeneous, both spatially as well as in frequency. Amplification factors reach values of up to 15 in Fig. 16c, d. After EQ12 amplification factors reach 20 (Fig. 16d). Note that neither the amplification factors nor the corresponding frequencies follow a simple pattern. As a general trend, however, it can be observed that rock slopes with higher degrees of damage exhibit larger amplification factors and stronger spatial heterogeneity.

8 Summary and Conclusions

Our study on seismic fatigue conceptually demonstrates how a sequence of earthquakes can bring a strong rock mass to collapse (catastrophic failure) over time by inducing incremental damage and deformation in a step-wise manner, until kinematic conditions become such that mobilization of the rock mass is possible. Although earthquakes are well recognized as key triggering factors, as the vast body of literature on earthquake-triggered rockslides demonstrates (e.g., Welkner et al. 2010; Moore et al. 2012; Parker 2013; Huang and Fan 2013, to name just several recent studies), their role as a preparatory factor (as conceptually illustrated in Fig. 1) is rarely described. In fact, the efficiency of earthquakes in reducing the rock mass strength and making the slope more susceptible to other driving mechanisms triggering catastrophic failure is substantial. Figure 14 shows that ground water pressure changes—although relatively strong in amplitude—were not able to induce significant damage over short time periods (i.e., 20 years) if the rock mass is not already in a

significantly damaged state. Only when the rock mass is in a highly damaged state do groundwater pressure changes become effective in inducing considerable displacements (after EQ10), or even triggering catastrophic failure (after EQ14). This illustrates an important characteristic of fatigue that has also been shown in laboratory experiments. Attewell and Farmer (1973) showed for rock samples that fatigue only leads to failure if a portion of the loading cycle brings stress above the damage (or crack) initiation limit. Analogous to these experiments, loading cycles in a rock mass at the slope scale can only be effective if incremental damage can be induced somewhere in the rock mass. During the progression of fatigue, strength is progressively reduced and hence, so is the limit above which further damage can be induced. In our case, simulated major earthquake events—even though they did not trigger catastrophic failure—reduced rock mass strength and raised criticality such that hydro-mechanical cycles became more damaging (Fig. 14). Similarly, subsequent earthquakes also became more damaging (Fig. 12).

In comparison to other fatigue processes, seismic fatigue occurs over a significantly longer time period, with repeat times for events far often exceeding the length of seismic records. This perhaps explains why seismic fatigue is rarely discussed (e.g., Bakun-Mazor et al. 2013). Hydro-mechanical, thermo-mechanical and freeze–thaw cycling occur on an annual basis (higher repeat frequency), inducing rock mass deformations and damage in smaller increments (lower amplitudes) and often only in limited parts of the rock mass. Large earthquakes, on the other hand, are rare (low repeat frequency) but rather violent strikes (higher amplitude). Also, the stress changes during such strikes involve the entire rock mass more or less equally, which is not the case for the aforementioned mechanisms that vary spatially in magnitude. Hydro-mechanical stress changes for instance are zero above the maximum groundwater table and can only reach considerable amplitudes below the minimum water table. In contrast seismically induced stress changes involve the entire rock mass and may even increase towards the surface due to various amplification phenomena (Gischig et al. 2015).

Seismic stability analysis methods described in the literature—ranging from simple pseudo-static analysis to Newmark's method to complex numerical analysis (Jibson 2011)—all require assumptions regarding the rock mass strength. However, damage induced by each earthquake reduces the rock mass strength. Considering seismic fatigue or any other fatigue process implies that rock mass strength is no longer a static property, but is subject to temporal change, i.e., progressive degradation. The effect of changing any driving or resisting force strongly depends on where the state of a slope is on a fatigue curve such as Fig. 1 or Fig. 9a. Hence, seismic stability assessment performed for current slope conditions have to be reconsidered once a moderate but potentially damaging earthquake strikes. The same ground motion used to assess slope stability can induce displacements varying over several orders of magnitude (Fig. 13). Accounting for such fatigue effects appropriately cannot rely on static stability analysis only, but requires advanced numerical modeling.

The fact that deformation rates responding to a driving mechanism depend on the damage and state of criticality of a rock mass has implications for the interpretation of monitoring data. The relationship between deformation rates and driving mechanisms, such as groundwater pressure changes, can give insight into the criticality of the rock slope, and thus can be used to calibrate numerical models (e.g., Gischig et al. 2011b, c). The state of damage and criticality established in the calibrated model can then be considered more realistic than simple static limit equilibrium assumptions of stability. We also highlight that the seismic response of a slope, for example the amplification or polarization characteristics (Burjánek et al. 2010, 2012; Gischig et al. 2015), presents another valuable means to further constrain the damage state of a rock slope model. Amplification factors of seismic waves and corresponding frequencies are very sensitive to changes in the network of open tension cracks (Fig. 16), and may be used as a diagnostic tool for slope criticality.

References

Attewell PB, Farmer IW (1973) Fatigue behavior of rock. Int J Rock Mech Min Sci Geomech Abstr 10(1):1–9

Bakun-Mazor D, Hatzor YH, Glaser SD, Santamarina JC (2013) Thermally vs. seismically induced block displacements in Masada rock slopes. Int J Rock Mech Min Sci 61:196–211

Bonzanigo L, Eberhardt E, Loew S (2007) Long-term investigation of a deep-seated creeping landslide in crystalline rock. Part I: geological and hydromechanical factors controlling the Campo Vallemaggia landslide. Can Geotech J 44(10):1157–1180

Bourdeau C, Havenith H-B (2008) Site effects modeling applied to the slope affected by the Suusamyr earthquake (Kyrgyzstan, 1992). Eng Geol 97:126–145

Bradley JJ, Fort AN, Jr (1966) Internal friction in rocks. In: Clark SP (ed) Handbook of physical constants. Geological Society of America, Boulder, pp 175–193

Burjánek J, Gassner-Stamm G, Poggi V, Moore JR, Fäh D (2010) Ambient vibration analysis of an unstable mountain slope. Geophys J Int 180(2):820–828

Burjánek J, Moore JR, Molina FXY, Faeh D (2012) Instrumental evidence of normal mode rock slope vibration. Geophys J Int 188:559–589

Christianson M, Board M, Rigby D (2006) UDEC simulation of triaxial testing of lithophysal tuffs. In: Proceedings of the 41st US rock mechanics symposium, ARMA-06-968

Crosta GB, Imposimato TS, Roddeman D, Chiesa S, Moia F (2005) Small fast-moving f low-like landslides in volcanic deposits: the 2001 Las Colinas landslide (El Salvador). Eng Geol 79:185–214

Cundall PA, Hart RD (1992) Numerical modelling of discontinua. Eng Comp 9:101–113

Eberhardt E (2008) Twenty-ninth Canadian Geotechnical Colloquium: the role of advanced numerical methods and geotechnical field measurements in understanding complex deep-seated rock slope failure mechanisms. Can Geotech J 45(4):484–510

Eberhardt E, Stead D, Coggan JS (2004) Numerical analysis of initiation and progressive failure in natural rock slopes—the 1991 Randa rockslide. Int J Rock Mech Min Sci 41:69–87

Eberhardt E, Bonzanigo L, Loew S (2007) Long-term investigation of a deep-seated creeping landslide in crystalline rock. Part II: mitigation measures and numerical modelling of deep drainage at Campo Vallemaggia. Can Geotech J 44(10):1181–1199

Evans SG, Bent AL (2004) The Las Colinas landslide, Santa Tecla: a highly destructive flowslide triggered by the January 13, 2001, El Salvador earthquake. In: Rose WI, Bommer JJ, Lopez DL, Carr MJ, Major JJ (eds) Natural hazards in El Salvador. Special Paper, Geological Society of America, Boulder, vol 375, pp 25–38

Fäh D, Moore JR, Burjanek J, Iosifescu I, Dalguer L, Dupray F, Michel C, Woessner J, Villiger A, Laue J, Marschall I, Gischig V, Loew S, Marin A, Gassner G, Alvarez S, Balderer W, Kästli P, Giardini D, Iosifescu C, Hurni L, Lestuzzi P, Karbassi A, Baumann C, Geiger A, Ferrari A, Laloui L, Clinton J, Deichmann N (2012) Coupled seismogenic geohazards in alpine regions. Bolletino di Geofisica Teorica ed Applicata 53(4):485–508

Fritsche S, Fäh D (2009) The 1946 magnitude 6.1 earthquake in the Valais: site-effects as a contributor to the damage. Swiss J Geosci 102:423–439

Fritsche SFD, Gisler M, Giardini D (2006) Reconstructing the damage field of the 1855 earthquake in Switzerland: historical investigations on a well-documented event. Geophys J Int 166:719–731

Gao FQ, Stead D (2014) The application of a modified Voronoi logic to brittle fracture modelling at the laboratory and field scale. Int J Rock Mech Min Sci 68:1–14

Gischig VS, Moore JR, Evans KF, Amann F, Loew S (2011a) Thermomechanical forcing of deep rock slope deformation: 1. conceptual study of a simplified slope. J Geophys Res Earth Surf 116:F04010

Gischig VS, Moore JR, Evans KF, Amann F, Loew S (2011b) Thermomechanical forcing of deep rock slope deformation: 2. the Randa rock slope instability. J Geophy Res Earth Surf 116:F04011

Gischig V, Amann F, Moore JR, Loew S, Eisenbeiss H, Stempfhuber W (2011c) Composite rock slope kinematics at the current Randa instability, Switzerland, based on remote sensing and numerical modeling. Eng Geol 118:37–53

Gischig V, Eberhardt E, Moore JR, Hungr O (2015) On the seismic response of deep-seated rock slope instabilities—insights from numerical modelling. Eng Geol 193:1–18

Gunzburger Y, Merrien-Soukatchoff V, Guglielmi Y (2005) Influence of daily surface temperature fluctuations on rock slope stability: case study of the Rochers de Valabres slope (France). Int J Rock Mech Min Sci 42:331–349

Hadley JB (1964) Landslides and related phenomena accompanying the Hegben Lake earthquake of August 17, 1959. United States Geological Survey Professional Paper 435-K, pp 107–138

Hansmann J, Loew S, Evans K (2012) Reversible rock slope deformations caused by cyclic water table fluctuations in mountain slopes of the Central Swiss Alps. Hydrogeol J 20:73–91

Heincke B, Maurer H, Green AG, Willenberg H, Spillmann T, Burlini L (2006) Characterizing an unstable mountain slope using shallow 2D and 3D seismic tomography. Geophysics 71(6):B241–B256

Heynen M (2010) Einfluss lokaler Geländegegebenheiten auf die seismische Stabilität eines Felshanges (Seetalhorn, VS). Master's thesis, ETH Zurich, Switzerland

Hoek E, Diederichs MS (2006) Empirical estimation of rock mass modulus. Int J Rock Mech Min Sci 43:203–215

Huang R, Fan X (2013) The landslide story. Nat Geosci 6:325–326

Hungr O, Leroueil S, Picearelli L (2014) The Varnes classification of landslide types, an update. Landslides 11(2):167–194

Itasca (2011) UDEC—Universal Distinct Element Code, Version 5.0 User's Manual. Itasca Consulting Group, Inc., Minneapolis

Jibson RW (2007) Regression models for estimating coseismic landslide displacement. Eng Geol 91:209–218

Jibson RW (2011) Methods for assessing the stability of slopes during earthquakes—a retrospective. Eng Geol 122:43–50

Jibson RW, Rathje EM, Jibson MW, Lee YW (2013) SLAMMER—Seismic LAndslide Movement Modeled using Earthquake Records. US Geological Survey Techniques and Methods

Jörg T (2008) Versagensmechanismus und Disposition des Medji Felssturz (Mattertal, Wallis). Master's Thesis, ETH Zurich, Switzerland

Kuhlemeyer RL, Lysmer J (1973) Finite element method accuracy for wave propagation problems. J Soil Mech Found Div, ASCE 99:421–427

Ladner F, Rovina H, Pointner E, Dräyer B, Sambeth U (2004) Ein angekündigter Felssturz. Geologische Überwachung und Instrumentierung des Felssturzes « Medji » bei St. Niklaus (Wallis), tec21, vol 27–28, pp 10–14

Lorig LJ, Cundall PA (1987) Modeling of reinforced concrete using the distinct element method. In: SEM/RILEM International conference on fracture of concrete and rock, Houston, pp 276–287

Macfarlane DF, Gillon MD (1996) The performance of landslide stabilization measures, Clyde power project, New Zealand. In: Senneset (ed) Proceedings of the 7th international symposium on landslides, Trondheim. Balkema, Rotterdam, vol 3, pp 1747–1757

Martin CD, Alzo'ubi AK, Cruden DM (2011) Progressive failure mechanisms in a slope prone to toppling. In: Slope Stability 2011 (ed) International symposium on rock slope stability in open pit mining and civil engineering, September 18–21, 2011, Vancouver

Moore JR, Gischig VS, Burjanek J, Loew S, Faeh D (2011) Site effects in unstable rock slopes: dynamic behavior of the Randa instability (Switzerland). Bull Seismol Soc Am 101(6):3110–3116

Moore JR, Gischig V, Amann F, Hunziker J, Burjanek J (2012) Earthquake-triggered rock slope failures: Damage and site effects. In: Eberhardt E, Froese C, Turner AK, Leroueil S (eds) Proceedings of the 11th international symposium on landslides. CRC Press, Banff, pp 869–874

Newmark NM (1965) Effects of earthquakes on dams and embankments. Geotechnique 15:139–159

Parker RN (2013) Hillslope memory and spatial and temporal distributions of earthquake-induced landslides. PhD thesis, Durham University

Parker RN, Petley D, Densmore A, Rosser N, Damby D, Brain M (2013) Progressive failure cycles and distributions of earthquake-triggered landslides. In: Ugai K, Yagi H, Wakai A (eds) Proceedings of the international symposium on earthquake induced landslides, Kiryu, Japan, 2012. Springer, New York

Petley D (2008) The Sichuan earthquake. Geogr Rev 22:2–4

Plafker G, Ericksen GE (1978) Nevados Huascaran avalanches. In: Voight B (ed) Rockslides and Avalanches, 1, Natural Phenomena. Elsevier, Amsterdam, pp. 277–314

Preisig G, Eberhardt E, Smithyman M, Preh A, Bonzanigo L (2015) Hydromechanical rock mass fatigue in deep-seated landslides accompanying seasonal variations in pore pressures. Rock Mech Rock Eng (in review)

Rovina (2005) St.Niklaus, Wallis: Unneri Spssplatte, Felsrutschung und Felssturz vom 21.11.2002. Unpublished report by Rovina + Partner, Büro für Ingenieurgeologie, 3953 Varen

Sartori M, Baillifard F, Jaboyedoff M, Rouiller JD (2003) Kinematics of the 1991 Randa rockslides (Valais, Switzerland). Nat Hazards Earth Syst Sci 3:423–433. doi:10.5194/nhess-3-423-2003

Schindler C, Cuénod Y, Eisenlohr T, Joris CL (1993) Die Ereignisse vom 18. April und 9. Mai 1991 bei Randa (VS): ein atypischer Bergsturz in Raten. Eclogae Geol Helv 86(3):643–665

Schorlemmer D, Wiemer S, Wyss M (2005) Variations in earthquake size distribution across different stress regimes. Nature 437:539–542

Watson AD, Moore DP, Stewart TW (2004) Temperature influence on rock slope movements at checkerboard creek. In: Lacerda WA et al (eds) Proceedings of the ninth international symposium on landslides. Taylor and Francis, Rio de Janeiro, pp 1293–1298

Watson AD, Psutka JF, Steward TW, Moore DP (2007) Investigations and monitoring of rock slopes at Checkerboard Creek and Little Chief Slide. In: Eberhardt E, Stead D, Morrison T (eds) Proceedings of the 1st Canada–US Rock Mechanics Symposium, Vancouver, pp 1015–1022

Welkner D, Eberhardt E, Hermanns RL (2010) Hazard investigation of the Portillo Rock Avalanche site, central Andes, Chile, using an integrated field mapping and numerical modelling approach. Eng Geol 114:278–297

Willenberg H (2004) Geologic and kinematic model of a complex landslide in crystalline rock (Randa, Switzerland). DSc thesis, ETH Zürich, Switzerland

Wolter A, Gischig V, Stead D, Clague JJ (2015) Investigation of geomorphic and seismic effects on the 1959 Madison Canyon, Montana landslide using an integrated field, engineering geomorphology mapping, and numerical modelling approach. Rock Mech Rock Eng (in review)

Xiao J-Q, Ding D-X, Xu G, Jiang F-L (2009) Inverted S-shaped model for nonlinear fatigue in rock. Int J Rock Mech Min Sci 46:643–648

Yin Y, Zheng W, Li X, Sun P, Li B (2011) Catastrophic landslides associated with the M8.0 Wenchuan earthquake. Bull Eng Geol Environ 70:15–32

Yugsi Molina FX (2010) Structural control of multi-scale discontinuities on slope instabilities in crystalline rock (Matter valley, Switzerland). DSc thesis, ETH Zurich, Switzerland

Zangerl C, Eberhardt E, Perzlmaier S (2010) Kinematic behaviour and velocity characteristics of a complex deep-seated crystalline rockslide system in relation to its interaction with a dam reservoir. Eng Geol 112:53–67